Computational Investigations of Nanophotonic Systems

by

Prashanth Sanjeev Venkataram

Submitted to the Department of Physics
in partial fulfillment of the requirements for the degree of

Bachelor of Science

at the

MASSACHUSETTS INSTITUTE OF TECHNOLOGY

June 2014

Signature redacted

Author ....
Department of Physics
2014 May 9

Signature redacted

Certified by..... .....
Marin Soljačić
Thesis Supervisor, Department of Physics
Thesis Supervisor

Signature redacted

Accepted by..... .....
Professor Nergis Mavalvala
Senior Thesis Coordinator, Department of Physics

Computational Investigations of Nanophotonic Systems

by

Prashanth Sanjeev Venkataram

Submitted to the Department of Physics
on 2014 May 9, in partial fulfillment of the
requirements for the degree of
Bachelor of Science

Abstract

In this thesis, I developed code in the MEEP finite-difference time domain classical electromagnetic solver to simulate the quantum phenomenon of spontaneous emission and its enhancement by a photonic crystal. The results of these simulations were favorably cross-checked with semianalytical predictions and experimental results. This code was further extended to simulate spontaneous emission from the top half of a sphere, where the top half is a dielectric material and the bottom half is a metal, in order to determine how effective the metal is at reflecting the emission toward the top. Separately, I used the SCUFF-EM boundary element method classical electromagnetic solver to simulate absorption and scattering, together called extinction, of infrared light from nanoparticles, and used those results to optimize the nanoparticle shapes and sizes for extinction at the desired infrared wavelength.

Thesis Supervisor: Marin Soljačić
Title: Thesis Supervisor, Department of Physics

Acknowledgments

Foremost, I would like to thank Prof. Marin Soljačić for taking me on as an undergraduate research student in 2011. I never knew what a wonderful world of research existed in photonics, and now thanks to this opportunity, I am going to attend graduate school for research in photonics or related areas. He has been an irreplaceable source of advice, from finding people in the group whose research I might find interesting, to taking the GREs and applying to graduate schools.

I would like to thank Prof. Peter Bermel (at Purdue University) for directly supervising me in my first research project under Prof. Soljačić regarding enhancing solar cell absorptivity through quasiperiodic texturing. Although that project is not included in this thesis, it was an invaluable first experience in university research for me, teaching me about the fundamentals of photonics, computational science, and even firsthand the process of science itself.

I would like to thank Prof. Alejandro Rodriguez (now at Princeton University) as well as Bo Zhen for supervising me in the photonic crystal project. They have taught me so much about photonic crystals and the relations between spontaneous emission & fluctuational electrodynamics. More than that, they have been completely supportive of me, whether my day has been good or bad, and whether my simulation results have looked promising or like trash. As if all of that weren't enough, they have advised me regarding graduate schools and even chatted with me about random topics in physics.

Finally, I would like to thank Dr. Owen Miller for supervising me in the nanoparticle scattering project. Even before I formally started doing research with him, he was happy to read through my graduate school and fellowship applications and discuss how a project with him could be carried out in the short- and long-terms. He taught me a whole lot about classical electromagnetic scattering as well as the differences between electromagnetic computational methods. Most of all, he was able to help me write this thesis.

Contents

List of Figures

List of Tables

Chapter 1

Maxwell's Equations and Computational Methods

1.1 Maxwell's Equations and Solvable Systems

The evolution and propagation of light is governed by Maxwell's equations, which in a general medium can be written as

$$\nabla \cdot \mathbf{D} = \rho_{\mathrm{f}} \tag{1.1}$$

$$\nabla \cdot \mathbf{B} = 0 \tag{1.2}$$

$$\nabla \times \mathbf{E} = -\frac{1}{c}\frac{\partial \mathbf{B}}{\partial t} \tag{1.3}$$

$$\nabla \times \mathbf{H} = \frac{1}{c}\left(\mathbf{J}_{\mathrm{f}} + \frac{\partial \mathbf{D}}{\partial t}\right) \tag{1.4}$$

where Lorentz-Heaviside units have been employed to allow the electric flux density $\mathbf{D}$, magnetic flux density $\mathbf{B}$, electric field $\mathbf{E}$, and magnetic field $\mathbf{H}$ to all have the same units. A further consequency of this choice of units is that the vacuum permittivity and permeability are set to unity: $\epsilon_0 = \mu_0 = 1$. Maxwell's equations can be used in

conjunction with the constitutive relations

$$\mathbf{D} = \epsilon \cdot \mathbf{E} \tag{1.5}$$

$$\mathbf{B} = \mu \cdot \mathbf{H} \tag{1.6}$$

to provide a full theory of electrodynamics in a material medium. In general, ϵ and μ may be functions of position $\mathbf{x}$ (inhomogeneity) or frequency ω (dispersion), in which case the constitutive relations hold at every individual position and frequency. Additionally, ϵ and μ may be complex, where the imaginary part is indicative of losses in the system. Finally, anisotropies may make ϵ and μ into two-index tensors, and nonlinearities may make ϵ and μ depend explicitly on the fields $\mathbf{E}$ and $\mathbf{H}$, though for the rest of this thesis, anisotropic and nonlinear materials will both be neglected. In principle, given sources ρ_f and $\mathbf{J}_f$ and boundary conditions on the fields, it should be possible to turn the crank of Maxwell's equations to show how all the fields evolve in space and time. There are two examples of this to motivate the rest of this thesis.

The first example is of a general photonic crystal. Much of this material is adapted from [8] with some further assumptions to better reflect the systems being considered here. It is convenient to assume that there are no free charge or current sources in the spatial region of interest, that $\mu = 1$ for every position and frequency, and that ϵ is real & positive to ignore losses for the moment (though the assumption about ϵ can be relaxed without much added difficulty). With those assumptions in mind, and only considering a monochromatic wave so that only the dependence of ϵ on position is relevant (but without making further assumptions at the moment regarding how ϵ varies with position), then Maxwell's equations become

$$\nabla \cdot (\epsilon(\mathbf{r})\mathbf{E}(\mathbf{r},t)) = 0 \tag{1.7}$$

$$\nabla \cdot \mathbf{H}(\mathbf{r},t) = 0 \tag{1.8}$$

$$\nabla \times \mathbf{E}(\mathbf{r},t) = -\frac{1}{c}\frac{\partial \mathbf{H}(\mathbf{r},t)}{\partial t} \tag{1.9}$$

$$\nabla \times \mathbf{H}(\mathbf{r},t) = \frac{\epsilon(\mathbf{r})}{c}\frac{\partial \mathbf{E}(\mathbf{r},t)}{\partial t} \tag{1.10}$$

under these conditions. The reason why only the spatial dependence and not the dispersion relation of ϵ needs to be considered is because only a monochromatic wave (constant ω) is being considered. That is because any function can be written as a superposition

$$\mathbf{X}(\mathbf{r},t) = \frac{1}{\sqrt{2\pi}} \int_{-\infty}^{\infty} \mathbf{X}(\mathbf{r},\omega) e^{-i\omega t}\, d\omega \tag{1.11}$$

so picking out a particular frequency ω simply means that

$$\mathbf{X}(\mathbf{r},t) = \mathbf{X}(\mathbf{r}) e^{-i\omega t} \tag{1.12}$$

for these electromagnetic fields $\mathbf{X} \in \{\mathbf{E}, \mathbf{H}\}$ (where the factor of $(2\pi)^{-\frac{1}{2}}$ has been absorbed into the spatial dependence of the vector field).

Once that has all been done, these fields can be plugged into Maxwell's equations, yielding

$$\nabla \cdot (\epsilon(\mathbf{r})\mathbf{E}(\mathbf{r})) = 0 \tag{1.13}$$

$$\nabla \cdot \mathbf{H}(\mathbf{r}) = 0 \tag{1.14}$$

as the transversality conditions, and

$$\nabla \times \mathbf{E}(\mathbf{r}) = \frac{i\omega}{c} \mathbf{H}(\mathbf{r}) \tag{1.15}$$

$$\nabla \cdot \mathbf{H}(\mathbf{r}) = -\frac{i\omega}{c} \epsilon(\mathbf{r}) \mathbf{E}(\mathbf{r}) \tag{1.16}$$

as the results of the dynamical equations. Eliminating $\mathbf{E}(\mathbf{r})$ from these conditions yields a general eigenvalue equation

$$\nabla \times (\epsilon^{-1}(\mathbf{r}) \nabla \times \mathbf{H}(\mathbf{r})) = \left(\frac{\omega}{c}\right)^2 \mathbf{H}(\mathbf{r}) \tag{1.17}$$

which is the master equation for the magnetic field in a general configuration of media determined by the position-dependent $\epsilon(\mathbf{r})$. The operator

$$\nabla \times (\epsilon^{-1}(\mathbf{r}) \nabla \times)$$

can be shown to be Hermitian, so the eigenvalues $\left(\frac{\omega}{c}\right)^2$ are real, and can further be shown to be nonnegative because ϵ is positive throughout space.[1]

If ϵ is chosen to be a periodic function of position – that is, if $\epsilon(\mathbf{r}+\mathbf{R}) = \epsilon(\mathbf{r})$ for a countably infinite set of translation vectors $\mathbf{R}$ that are linear superpositions of lattice basis vectors – then the linear operator

$$\nabla \times (\epsilon^{-1}(\mathbf{r})\nabla\times)$$

is also periodic with the same periodicity in space. By Bloch's theorem, this means that the magnetic field eigenfunctions can be written as

$$\mathbf{H}_\mathbf{k}(\mathbf{r}) = e^{i\mathbf{k}\cdot\mathbf{r}}\mathbf{u}_\mathbf{k}(\mathbf{r}) \tag{1.18}$$

where $\mathbf{k}$ is a wavevector lying within the irreducible Brillouin zone (henceforth called simply the Brillouin zone for brevity) of the reciprocal to the lattice defining $\epsilon(\mathbf{r})$. Moreover, $\mathbf{u}_\mathbf{k}(\mathbf{r})$ is a vector function that is periodic in position in the same way that $\epsilon(\mathbf{r})$ is, meaning that $\mathbf{u}_\mathbf{k}(\mathbf{r}+\mathbf{R}) = \mathbf{u}_\mathbf{k}(\mathbf{r})$ for the same countably infinite set of $\mathbf{R}$ as before. Such a system is called a photonic crystal, because the dielectric function repeats itself in space according to a crystal lattice structure. A key feature of the photonic crystal is the existence of a photonic band gap, in analogy with the electronic bandgap in a semiconductor crystal. This analogy can be taken further in the specific case of a simple 1-dimensional photonic crystal, where the dielectric function is an alternating layering of two different materials. If the layers were in fact the same material so the dielectric slab was uniform, there would be continuous translational symmetry, and all frequencies would be accessible for all wavevectors as there would be no Brillouin zone. However, introducing a discrete translational symmetry breaks the continuous translational symmetry and shrinks the set of states to lie within the Brillouin zone; the frequency bands as functions of $\mathbf{k}$ must fold upon themselves

[1]The inverse dielectric ϵ^{-1} is the reciprocal of ϵ, or if there are anisotropies, the inverse matrix of ϵ; it is not the mathematical inverse function of $\epsilon(\mathbf{r},\omega)$ (which is impossible for a function of multiple arguments anyway).

to fit in this zone, and introducing the discrete translational symmetry causes gaps to emerge between different bands. No electromagnetic field states (wavevectors $\mathbf{k}$, without considering polarization for the moment) may exist for frequencies in those gaps. The existence of photonic band gaps has been a relatively recent discovery showing the novel ways that electromagnetic waves can be manipulated, and has led to other discoveries such as enhancement of absorption or reflection at certain wavelengths, and as will be discussed in this thesis, enhancement of spontaneous emission.

The second example of an exactly solvable system is electromagnetic scattering from a dielectric sphere of radius a and dielectric constant ϵ sitting in a vacuum. Here it is assumed that ϵ is homogeneous within the sphere, though it may be lossy (and the dispersion relation is ignored by considering only monochromatic fields). This derivation is adapted from [3] where the only further assumption that has been made is that $\mu = 1$, which is reflective of the materials that will be considered later in this thesis as well. For time-harmonic electromagnetic fields with no free charges or currents, Maxwell's equations read

$$\nabla \cdot \mathbf{E}(\mathbf{r}) = 0 \tag{1.19}$$

$$\nabla \cdot \mathbf{H}(\mathbf{r}) = 0 \tag{1.20}$$

$$\nabla \times \mathbf{E}(\mathbf{r}) = \frac{i\omega}{c}\mathbf{H}(\mathbf{r}) \tag{1.21}$$

$$\nabla \times \mathbf{H}(\mathbf{r}) = -\frac{i\omega\epsilon(\mathbf{r})}{c}\mathbf{E}(\mathbf{r}) \tag{1.22}$$

where $\epsilon(\mathbf{r})$ is a step function changing between the desired homogeneous ϵ inside the sphere and 1 outside the sphere (which is the surrounding vacuum). These equations combine to give the Helmholtz equations $\nabla^2\mathbf{X}(\mathbf{r}) + k^2\mathbf{X}(\mathbf{r}) = 0$ for $\mathbf{X} \in \{\mathbf{E}, \mathbf{H}\}$ where $k^2 = \frac{\omega^2\epsilon(\mathbf{r})}{c^2}$. It turns out that the general vectors $\mathbf{M}(\mathbf{r}) = \nabla \times (\mathbf{r}\psi(\mathbf{r}))$ and $\mathbf{N}(\mathbf{r}) = \frac{1}{k}\nabla \times \mathbf{M}(\mathbf{r})$ can act as electromagnetic fields as well, provided that ψ also satisfies the Helmholtz equation $\nabla^2\psi(\mathbf{r}) + k^2\psi(\mathbf{r}) = 0$. It can be shown that the even

solutions ('e') and odd solutions ('o') for ψ can be written as

$$\psi_{emn}(\mathbf{r}) = z_n(kr)P_{mn}(\cos(\theta))\cos(m\varphi) \tag{1.23}$$

$$\psi_{omn}(\mathbf{r}) = z_n(kr)P_{mn}(\cos(\theta))\sin(m\varphi) \tag{1.24}$$

where z_n is a spherical Bessel function (j_n or y_n, or the linear combinations yielding the spherical Hankel functions $h_n^{(1)}$ or $h_n^{(2)}$) of order n and P_{mn} is an associated Legendre function of order (m, n). For the remainder of this derivation, the argument $\mathbf{r}$ will be made implicit for brevity. Here, m and n are both integers satisfying $m \geq 0$ and $n \geq m$. The spherical Bessel functions, associated Legendre functions, and trigonometric functions each satisfy completeness and orthogonality relations; these should be true because the Helmholtz equation is an eigenvalue equation for the Hermitian operator $-\nabla^2$, and every Hermitian operator has a complete & orthonormal eigenbasis along with real eigenvalues. In terms of these, the definitions of the vector normal modes of the sphere $\mathbf{M}_{emn}$, $\mathbf{M}_{omn}$, $\mathbf{N}_{emn}$, and $\mathbf{N}_{omn}$ follow from the relations of $\mathbf{M}$ to ψ and of $\mathbf{N}$ to $\mathbf{M}$.

In terms of these, it can be shown that an incident plane wave electric field

$$\mathbf{E}_{\text{inc}} = E_0 e^{ikr\cos(\theta)}\mathbf{e}_x \tag{1.25}$$

can be expanded in terms of vector normal modes of the sphere as

$$\mathbf{E}_{\text{inc}} = E_0 \sum_{n=1}^{\infty} i^n \frac{2n+1}{n(n+1)} \left(\mathbf{M}_{o1n}^{(1)} - i\mathbf{N}_{e1n}^{(1)}\right) \tag{1.26}$$

where the superscript (1) indicates use of j_n rather than any of the other spherical Bessel function types (y_n, $h_n^{(1)}$, or $h_n^{(2)}$). The boundary conditions are that the tangential components of $\mathbf{E}$ and $\mathbf{H}$ must be continuous across the boundary of the sphere, where the total fields outside are the sums of incident and scattered fields. Enforcing

these boundary conditions means that the scattered electric field is

$$\mathbf{E}_{\text{sca}} = E_0 \sum_{n=1}^{\infty} i^n \frac{2n+1}{n(n+1)} \left(i a_n \mathbf{N}_{e1n}^{(3)} - b_n \mathbf{M}_{o1n}^{(3)} \right) \tag{1.27}$$

where the superscript (3) indicates use of the particular Hankel function $h_n^{(1)}$, with $\mathbf{H}_{\text{sca}}$ found according to $\nabla \times \mathbf{E} = ik\mathbf{H}$. By further enforcing the boundary conditions and orthogonality relations, the scattering coefficients a_n and b_n can finally be written in terms of the Riccati-Bessel functions

$$\phi_n(x) = x j_n(x) \tag{1.28}$$

$$\xi_n(x) = x h_n^{(1)}(x) \tag{1.29}$$

(where the letter ϕ has been used instead of ψ to avoid confusion with ψ_{emn} and ψ_{omn} from above) as

$$a_n = \frac{m\phi_n(mx)\phi_n'(x) - \phi_n(x)\phi_n'(mx)}{m\phi_n(mx)\xi_n'(x) - \xi_n(x)\phi_n'(mx)} \tag{1.30}$$

$$a_n = \frac{\phi_n(mx)\phi_n'(x) - m\phi_n(x)\phi_n'(mx)}{\phi_n(mx)\xi_n'(x) - m\xi_n(x)\phi_n'(mx)} \tag{1.31}$$

where here $x = ka$ is the product of the sphere radius with the wavenumber in the vacuum, m is (possibly complex) sphere index of refraction, and primes denote derivatives evaluated at the specified argument.

Only very special cases of these systems, such as modes of a one-dimensional lossless photonic crystal, or scattering from a homogeneous dielectric sphere, can be described analytically. Otherwise, in general, computational methods are needed. Two of them in particular are described below.

1.2 MEEP

The MIT Electromagnetic Equation Propagation software (MEEP) is one of many computational electromagnetic solvers available, as detailed in [11]. It is a finite-

difference time domain (FDTD) algorithm, which means that it discretizes space and time into a lattice, sets up the sources and boundary conditions, and discretely evolves the fields in space and time through Maxwell's equations. In particular, an FDTD approach discretizes space into a lattice spaced by the resolution a and time into steps τ as well, so that derivatives in space

$$\frac{\partial v(x,y,z,t)}{\partial x} \approx \frac{v(x+a,y,z,t) - v(x-a,y,z,t)}{2a}$$

and in time

$$\frac{\partial v(x,y,z,t)}{\partial t} \approx \frac{v(x,y,z,t+\tau) - v(x,y,z,t-\tau)}{2\tau}$$

are finite differences for any quantity v. This way, the differential Maxwell equations become difference equations, which can be solved given boundary conditions in space and time through recursion. The particular boundaries may include sources, initial field profiles, computational cell boundaries such as metallic walls, or dielectrics within the computational cell.

There are three small subtleties to be addressed with regard to the discretization of space and time. The first is that MEEP discretizes time in much the same way that it discretizes space. Because it sets $c = 1$ (as further discussed below), space and time are considered to be of the same units, so the time resolution is simply related to the spatial resolution by a constant prefactor. This is called the Courant factor, and all calculations used in this thesis set the Courant factor to $\frac{1}{2}$, so that the number of time steps in a MEEP time unit is twice the number of spatial steps in a MEEP length unit.

The second is that MEEP uses a Yee lattice. In 3 dimensions, space is discretized into cubes called voxels centered on a point in the discrete computational lattice and with side length equal to the inverse of the spatial resolution (e.g. if the resolution is set to 10, so that there are 10 spatial steps in one MEEP length unit, then the side length of the voxel is $\frac{1}{10}$). Ordinarily, the fields might all be computed at center of the voxel. In MEEP, however, the electric field $\mathbf{E}$ and electric flux density $\mathbf{D}$ are both computed at the centers of the edges of the voxel, while the magnetic field

$\mathbf{H}$ and magnetic flux density $\mathbf{B}$ are both computed at the centers of square faces of the voxel. For one, this means that if the fields at a certain point are desired, interpolation must be carried out to account for the separation of the edges from each other or the faces from each other. For another, if derived quantities such as the Poynting flux $\mathbf{S} = \mathrm{Re}(\mathbf{E} \times \mathbf{H}^*)$ (when complex fields are used, and when $c = 1$) are desired, further interpolation must be done to account for the half-voxel offset between the edge centers and the face centers. The subtlety about the Courant factor as well as this subtlety are both very technical points, as the implications of the Courant factor and Yee lattice are not directly used, so they are never dealt with again in this thesis.

Regarding the last part, the third subtlety is that MEEP generally interpolates everywhere. One immediate consequences of this are that if point sources are desired but the point of interest does not directly lie on the discrete computational lattice, MEEP will put sources at the nearest lattice points to the desired point and weight the resulting sources by the distances of those lattice points from the desired point. Another is that MEEP performs subpixel averaging of the dielectric function by default, so sharp cutoffs or transitions in the the dielectric function from one region to another are smoothened. This subpixel averaging of the dielectric function is observed in the work done in this thesis, but generally does not pose problems *per se*.

Maxwell's equations are scale-invariant, meaning that multiplying the length and time scales by the same constant factor yields the same frequency eigenvalues and magnetic field eigenfunctions of the master equation 1.17 provided that the dielectric function is appropriately rescaled as well. For simple photonic crystals, this rescaling of the dielectric function may be the same constant factor at all positions, while for more complicated structures, the dielectric function may need to be rescaled differently at different points. This has the consequence that different dielectric functions at different length scales may produce the same eigenvalues and eigenfunctions, so if the desired goal is to produce a certain eigenfunction and eigenvalue pair, then the problem reduces to either fixing the dielectric spatial profile and determining at which length scale it should exist, or fixing the length scale and determining which dielectric

function will produce these modes. Because of this freedom, MEEP does not impose units on the user. It sets $c = 1$, and it makes all lengths and times be in units of the user-picked length scale a, all cyclic frequencies ν in units of a^{-1}, and all angular frequencies ω in units of $2\pi a^{-1}$. Moreover, because only linear systems are being considered (i.e. ϵ does not depend on the electromagnetic fields), the units of the fields themsleves are irrelevant, as usually the fields are used only to give dimensionless ratios such as transmission coefficients or flux enhancement factors.

Finally, the equations that MEEP ends up discretizing (in units where $c = 1$) are

$$\mathbf{D} = \epsilon \mathbf{E} \tag{1.32}$$

$$\mathbf{B} = \mu \mathbf{H} \tag{1.33}$$

$$\frac{\partial \mathbf{D}}{\partial t} = \nabla \times \mathbf{H} - \mathbf{J}_D - \sigma_D \mathbf{D} \tag{1.34}$$

$$\frac{\partial \mathbf{B}}{\partial t} = -\nabla \times \mathbf{E} - \mathbf{J}_B - \sigma_B \mathbf{B} \tag{1.35}$$

along with the general boundary conditions

$$\nabla \cdot \mathbf{D}(\mathbf{r}, t) = -\int_{t_0}^{t} \nabla \cdot (\mathbf{J}_D(\mathbf{r}, t') + \sigma_D \mathbf{D}(\mathbf{r}, t'))\, dt' \tag{1.36}$$

$$\nabla \cdot \mathbf{B}(\mathbf{r}, t) = -\int_{t_0}^{t} \nabla \cdot (\mathbf{J}_B(\mathbf{r}, t') + \sigma_B \mathbf{B}(\mathbf{r}, t'))\, dt' \tag{1.37}$$

where the particular value of t_0 does not actually matter. In general, the permittivity ϵ and permeability μ may depend on $\mathbf{r}$ and ω and may be anisotropic (but are usually assumed to be linear, though MEEP is capable of handling nonlinearities), and the electrical conductivity σ_D and magnetic conductivity σ_B may be functions of $\mathbf{r}$ but are independent of ω. Regarding that last point, $\mathbf{J}_D$ is the usual electric current density, while $\mathbf{J}_B$ is the magnetic current density; $\mathbf{J}_B$ may be interpreted literally as the current of moving magnetic monopoles, which do not exist but which can in many cases produce perfectly physical fields (giving an alternative and sometimes easier approach to deriving desired field profiles).Additionally, because the general boundary conditions involve integrals over time of the flux of current density, then

static electric or magnetic monopole sources may not be used, and dynamic electric or magnetic monopole sources are included in the current density definitions by way of the continuity equation $\nabla \cdot \mathbf{J} = -\frac{\partial \rho}{\partial t}$.

The remaining boundary conditions are specific for each problem that can be solved in MEEP. The computational cell must of course be a finite size, and conditions may be imposed along one or more axes upon the faces of the computational cell normal to those axes. One or more of the boundaries of the cell may be perfectly metallic in either field (σ_D or σ_B is infinite), meaning the fields go to zero at the metal walls. Alternatively, one or more axes of the cell may have associated periodic boundaries with wavevector $\mathbf{k}$ lying within the irreducible Brillouin zone (i.e. in $\pm\frac{\pi}{a}$ along the direction of the periodic boundaries, where a is the length of the computational cell in that direction), so that fields satisfy Bloch's theorem $\mathbf{X}(\mathbf{r} + \mathbf{R}) = e^{i\mathbf{k}\cdot\mathbf{r}}\mathbf{X}(\mathbf{r})$ where $\mathbf{R}$ is any integer superposition of basis vectors for the periodic lattice. Finally, one or more axes of the cell may have the faces of the cell normal to those axes covered with a finite thickness of perfectly matched layers (PML). PML does not exist in reality but only exists for computational convenience; it is a material that ramps on absorption/conductivity gradually over its thickness from the interior of the cell to the face of the cell, so that fields incident upon PML will be absorbed and only minimally reflected. Theoretically, PML should absorb any frequency of light incident at any angle without reflecting it, but empirically as implemented in MEEP, PML only works well for a small range of incidence angles. That said, because the systems studied in this thesis are not surrounded by metallic walls and do not have periodic boundaries along all axes, PML is the most realistic boundary condition along those axes that do not have periodic boundaries.

Beyond those standard boundaries, any material may be added anywhere in the computational cell forming even more boundary conditions. As described above, these materials may be lossy, dispersive, anisotropic, or conductive with regard $\mathbf{D}$ or $\mathbf{B}$. Further boundaries come in the form of sources. In MEEP, rather than specifying an initial field profile, the user can specify an initial current source profile. Each source can be either a point or an extended region, and each source is the product of

user-specified or built-in functions of space $\mathbf{J}(\mathbf{r})$ and time $f(t)$ so $\mathbf{J}(\mathbf{r},t) = \mathbf{J}(\mathbf{r})f(t)$. If a more complicated function that cannot be separated into spatial and temporal parts is desired, multiple sources, each with different spatial and temporal component functions, can be specified to exist at the same point or over the same region. Hence, MEEP essentially steps through Maxwell's equations in discrete form in a finite computational cell subject to all of the above conditions and restrictions.

1.3 SCUFF-EM

In contrast to MEEP, the Surface Current/Field Formulation of Electromagnetism (SCUFF-EM) solver uses the boundary element method (BEM) to solve electromagnetic problems [7, 1]. SCUFF-EM is primarily built to solve electromagnetic scattering problems, and the key to the operation of SCUFF-EM is the electromagnetic equivalence theorem. For this problem, it is necessary to consider linear, isotropic functions ϵ and μ, in which a boundary can be drawn that has a well-defined interior and exterior. Inside this boundary will exist volume currents $\mathbf{J}$ that produce electric fields $\mathbf{E}$ and magnetic fields $\mathbf{H}$; no volume magnetic currents exist because no magnetic monopoles exist. However, it is possible to replace these volume currents with surface electric currents $\mathbf{K}$ and surface magnetic currents $\mathbf{N}$ at the boundary, satisfying the boundary conditions $\mathbf{K} = \mathbf{n} \times \Delta\mathbf{H}$ and $\mathbf{N} = -\mathbf{n} \times \Delta\mathbf{E}$ in appropriate units. Here, $\Delta f \equiv f_{\text{out}} - f_{\text{in}}$ for any quantity f across a boundary, and $\mathbf{n}$ is the unit normal vector pointing to the exterior of the surface at each point along the surface. Moreover, because scattering problems such as those solved by SCUFF-EM are focused on determining scattered fields exterior to a particle, typically the interior fields are of less relevance than the exterior fields. This means that the interior fields can be absorbed into the surface current definitions, leaving $\mathbf{K} = \mathbf{n} \times \mathbf{H}_{\text{out}}$ and $\mathbf{N} = -\mathbf{n} \times \mathbf{E}_{\text{out}}$ as the redefined surface currents. Hence, the surface electric and magnetic currents are essentially rotations of the magnetic and electric fields, respectively, at the surface. For example, for a perfect electrical conductor, the magnetic current must vanish, so what is left is $\mathbf{N} = 0$ and $\mathbf{K} = \mathbf{n} \times \mathbf{H}_{\text{out}}$. Despite the facts

that magnetic monopoles do not exist and no physical current is completely confined to a surface, these fictitious surface currents do in fact reproduce the correct fields $\mathbf{E}$ and $\mathbf{H}$ everywhere outside of the boundary. SCUFF-EM can handle regions of homogeneous, isotropic, linear materials, so the surface currents are most naturally confined to the boundaries of these regions of different dielectric functions.

For classical electromagnetic scattering, SCUFF-EM first calculates the equivalent surface currents according to the equivalence theorem whose implications are outlined above. SCUFF-EM then determines the scattering Green's function for the given set of material regions and their boundaries; this Green's function is generalized to produce the (physical) fields from both (fictitious) surface electric and magnetic currents. Finally, this Green's function is convolved with the surface currents at each boundary, with the results added together to yield the scattered electromagnetic fields. SCUFF-EM discretizes the boundaries by triangular panels and expands surface currents in terms of vector basis functions along those panels, but this discretization along with other approximations performed in the computation of the scattering problem are largely hidden from the end-user once the relevant regions and surfaces are specified.

The method of using SCUFF-EM for solving the scattering problems considered in this thesis is as follows. The user creates a GEO file that represents the geometry of a boundary in consideration; this is usually a closed boundary of a solid object. The user then uses the GMSH tool to convert this into a MSH file containing information about how the surface is discretized. This is then incorporated into a SCUFFGEO file, which also contains information about the material properties (essentially just the dispersion relations $\epsilon = \epsilon(\omega)$ and $\mu = \mu(\omega)$) of the interior and exterior regions to the boundary. Finally, this SCUFFGEO file, along with information about the relevant frequencies to consider, as well as the polarization and direction of incident electromagnetic waves, is passed along to SCUFF-SCATTER (a subprogram of SCUFF-EM), which then solves the scattering problem given the geometric configuration and parameters; the results include, among other information, scattered and absorbed powers at each frequency. Note that SCUFF-EM uses different units in different contexts, though it consistently uses SI definitions of electromagnetic quantities in setting ϵ_0 and μ_0 to have nontrivial

numerical values. By making use of the scale-invariance of Maxwell's equations to set a length scale appropriate for scattering problems, all length scales, such as those specified in GEO files, are in terms of $a = 1\,\mu\text{m}$. This means that frequencies ω (and $\nu = \frac{\omega}{2\pi}$) passed into SCUFF-SCATTER are in terms of $\frac{c}{a} = \frac{c}{1\,\mu\text{m}}$, and the default incident electric field amplitude is $|\mathbf{E}_{\text{inc}}| = 1\,\frac{\text{V}}{\mu\text{m}}$, where the intensity of that field is $\frac{1}{2Z_0}|\mathbf{E}_{\text{inc}}|^2$ given the vacuum impedance $Z_0 = \sqrt{\frac{\mu_0}{\epsilon_0}} \approx 377\,\Omega$ in SI units. By contrast, the frequencies ω passed into the SCUFFGEO file are converted into SI units, so the functions $\epsilon(\omega)$ and $\mu(\omega)$ should be written with that in mind, although $\epsilon(\omega)$ and $\mu(\omega)$ are taken to be the relative permittivity and permeability, respectively, rather than the absolute quantities after multiplication by ϵ_0 or μ_0. Additionally, the scattered and absorbed powers are reported in SI units as well, so the cross section in $(\mu\text{m})^2$ is the power in SI units divided by the intensity described above.

Chapter 2

Spontaneous Emission and its Simulation

2.1 Spontaneous Emission and Enhancement in a Small Cavity

The first part of this thesis considers the enhancement of fluorescent emission by a photonic crystal. Generally, fluorescent emission is essentially spontaneous emission of light by atoms or molecules decaying from an excited state down to a ground state in which the excited state has a very short lifetime. From time-dependent perturbation theory, Fermi's golden rule gives

$$R_{e\to g} = \frac{4\pi^2}{3\hbar^2}|\vec{\mu}_{e,g}|^2\rho(\omega_{e,g}) \tag{2.1}$$

as the transition rate of molecules from an excited state e to the ground state g, where $\hbar\omega_{e,g}$ is the energy difference between the two states, $\vec{\mu}_{e,g}$ is the dipole matrix element for transitioning between the excited and ground states, and

$$\rho(\omega) = \frac{\hbar}{\pi^2 c^3}\frac{\omega^3}{e^{\frac{\hbar\omega}{k_B T}} - 1} \tag{2.2}$$

is the Planck distribution of intensity (density of states) as a function of frequency for light at thermal equilibrium with molecules in the excited and ground states at temperature T.

That said, this is just the rate of spontaneous emission of photons from excited molecules into the vacuum. As Purcell discovered, the rate of spontaneous emission depends not only on the molecules themselves but also on the surrounding environment, so if the molecules are placed in an optical cavity and if the frequency of photons spontaneously emitted is the same as that of a resonance in that cavity, then the rate of spontaneous emission will increase depending on the quality factor of the cavity as well as the volume of the resonance mode in that cavity.

For the particular example similar to what Purcell studied of a molecule in a small cavity of mirrors with a tiny hole inside, the Purcell enhancement is better described as an enhancement of the local density of states, because the cavity being so small and localized means that the density of states will depend not only on the frequency but also heavily on the position of observation outside of the cavity. Much of this derivation is adapted from [12] with the assumption that $\mu = 1$. The cavity will have resonances α with orthogonal (in α) electric eigenfields $\mathbf{E}^{(\alpha)}(\mathbf{r})$ and real eigenfrequencies $\omega_{(\alpha)}$ solving

$$\epsilon^{-1}(\mathbf{r})\nabla \times (\nabla \times \mathbf{E}^{(\alpha)}(\mathbf{r})) = \frac{\omega_{(\alpha)}^2}{c^2}\mathbf{E}^{(\alpha)}(\mathbf{r}) \tag{2.3}$$

where it has been assumed that $\mu = 1$ through all space. Whereas the density of states (DOS) is given by

$$\mathrm{DOS}(\omega) = \sum_{\alpha} \delta(\omega - \omega_{(\alpha)}) \tag{2.4}$$

assuming no degeneracies, the local density of states (LDOS) weights the summand by the energy density as

$$\mathrm{LDOS}(\mathbf{r}, \omega, l) = \sum_{\alpha} \delta(\omega - \omega_{(\alpha)})\epsilon(\mathbf{r})|E_l^{(\alpha)}(\mathbf{r})|^2 \tag{2.5}$$

where l is one of the three Cartesian directions. This way, if the energy density

contribution from one direction of the field vanishes at any point outside the cavity, then photon states also vanish locally at that point. In this case, the eigenfield normalization has been chosen such that

$$\int \mathbf{E}^{(\alpha)\star}(\mathbf{r}) \cdot \epsilon(\mathbf{r}) \mathbf{E}^{(\alpha)}(\mathbf{r})\, d^3r = 1$$

for convenience, so $\epsilon(\mathbf{r})|\mathbf{E}_l^{(\alpha)}(\mathbf{r})|^2$ is a *normalized* energy density contribution from fields along direction l.

That all describes free eigenfields with the cavity. If there are sources present, the cavity eigenfield equation is modified to be the inhomogeneous equation

$$\epsilon^{-1}\nabla \times (\nabla \times \mathbf{E}) - \frac{\omega^2}{c^2}\mathbf{E} = \frac{i\omega}{c^2}\epsilon^{-1}\mathbf{J} \tag{2.6}$$

where the source $\mathbf{J}(\mathbf{r})$ has no explicit time dependence remaining by virtue of assuming a time-harmonic source. In particular, because the Purcell enhancement is most simply stated as the radiation enhancement of a single point dipole when put in a cavity, it is useful to consider a point dipole current $\mathbf{J}(\mathbf{r}) = \delta(\mathbf{r} - \mathbf{r}_0)\mathbf{e}_l$ where $\mathbf{r}_0$ is the location of its dipole, $\mathbf{e}_l$ is the Cartesian direction of the dipole for a fixed $l \in \{1, 2, 3\}$, and the units are chosen so that the amplitude of the dipole is unity (and also that $c = 1$). Through a Green's function approach, this can be simply solved for the electric field in terms of the eigenfields of the cavity and their overlap with the source. However, the response fields diverge on resonance unless some loss is present with each resonance, and this loss can be written either as an imaginary part of the dielectric ($\mathrm{Im}(\epsilon) \neq 0$ and $\mathrm{Im}(\epsilon) \ll 1$) or as an imaginary part of the eigenfrequency ($\tilde{\omega}_{(\alpha)} = \omega_{(\alpha)} - i\gamma_{(\alpha)}$ with $\gamma_{(\alpha)} \ll \omega_{(\alpha)}$). Replacing $\omega_{(\alpha)}$ with $\tilde{\omega}_{(\alpha)}$ yields the response fields

$$\mathbf{E}(\mathbf{r}) = i\omega \sum_\alpha \frac{\mathbf{E}^{(\alpha)}(\mathbf{r})}{(\omega_{(\alpha)} - i\gamma_{(\alpha)})^2 - \omega^2} \int \mathbf{E}^{(\alpha)\star}(\mathbf{r}) \cdot \mathbf{J}(\mathbf{r})\, d^3r \tag{2.7}$$

$$= i\omega \sum_\alpha \frac{\mathbf{E}^{(\alpha)}(\mathbf{r})}{(\omega_{(\alpha)} - i\gamma_{(\alpha)})^2 - \omega^2} E_l^{(\alpha)}(\mathbf{r}_0) \tag{2.8}$$

where the first equality is generally true and the second equality is true for a point dipole current source along a given direction l. Plugging this into the equation for the total radiated and absorbed power (though the units are slightly different from power due to the field normalization choices)

$$P = -\frac{1}{2}\mathrm{Re}\left(\int \mathbf{E}^{\star}(\mathbf{r}) \cdot \mathbf{J}(\mathbf{r})\, d^3r\right) \tag{2.9}$$

for the point dipole source & response fields as given above and enforcing the assumptions of small loss yield

$$P_l \approx \frac{1}{4}\sum_{\alpha} \frac{\gamma_{(\alpha)}}{(\omega - \omega_{(\alpha)}^2 + \gamma_{(\alpha)}^2} |E_l^{(\alpha)}(\mathbf{r}_0)|^2 \tag{2.10}$$

as the total radiated and absorbed power. When the loss is zero, the Lorentzian peaks in the power become Dirac delta functions, in which case the total power becomes proportional to the local density of states at the location of the point dipole: $\mathrm{LDOS}(\mathbf{r_0}, \omega, l) \approx \frac{4}{\pi}\epsilon(\mathbf{r}_0) P_l(\mathbf{r}_0, \omega)$, where the approximation holds for small loss and becomes exact for vanishing loss. For small loss, picking a resonance α, examining the frequency exactly at $\omega = \omega_{(\alpha)}$, and summing over all three possible values of l to get the average LDOS from a randomly oriented dipole yields a contribution of $\frac{2Q_{(\alpha)}}{\pi\omega_{(\alpha)}V_{(\alpha)}}$ to the LDOS from that resonance, where

$$Q_{(\alpha)} = \frac{\omega_{(\alpha)}}{2\gamma_{(\alpha)}} \tag{2.11}$$

is the quality factor of the resonant mode, and

$$V_{(\alpha)} = \frac{\int \epsilon(\mathbf{r})|\mathbf{E}^{(\alpha)}(\mathbf{r})|^2\, d^3r}{\max\limits_{\mathbf{r}} \epsilon(\mathbf{r})|\mathbf{E}^{(\alpha)}(\mathbf{r})|^2} \tag{2.12}$$

is the mode volume of the resonant mode (where in this derivation the numerator of the mode volume is unity due to the normalization choice). Thus, the enhancement to the LDOS from placing the molecule inside a cavity is given by the factor $\frac{Q_{(\alpha)}}{V_{(\alpha)}}$ for a resonant mode α.

2.2 Spontaneous Emission Enhancement from a Photonic Crystal

As opposed to a small, localized resonant cavity as in Purcell's original analysis, the system being primarily considered in this thesis is a large photonic crystal slab which can support delocalized eigenfields with long electromagnetic lifetimes. This photonic crystal is among the first systems to support interactions between organic molecules and inorganic materials allowing for enhancement of spontaneous emission by the organic molecules. Such enhancement would be of immense use to imaging and sensing, both for further studies in fundamental photonics, as well as for applications to biology and biomedicine.

This photonic crystal, pictured in figure 2-1, has a band structure with multiple bands. This means that eigenfields must be labeled by both the continuous crystal momentum $\mathbf{k}$ within the first Brillouin zone as well as the corresponding resonant frequency $\omega_{\mathbf{k}}$ to fully specify the mode. The photonic crystal in question is a rectangular slab of silicon nitride (Si_3N_4) with circular holes made at the centers of square unit cells; the slab is 250 nm thick. In the experiments done on this system, the holes have been drilled 55.5 nm from the top surface down. The photonic crystal is bonded on top of a substrate of silicon dioxide (SiO_2), and the whole system is immersed in a 1 millimolar solution of active rhodamine 6G (R6G) dye molecules in passive methanol, where the methanol-R6G solution fills the shallow holes and forms a 2 μm-thick layer above the photonic crystal.

Because the methanol solution is uniform and isotropic above the photonic crystal, and because multiple bands exist in the band structure, it makes less sense to discuss the LDOS here, as position is less relevant for a slab that is periodic and almost infinitely large in 2 dimensions compared to the size of a detector. Instead, the spectral density of states, which considers the states available to photons at a particular direction given by the crystal momentum $\mathbf{k}$ (within the first Brillouin zone) and corresponding resonant frequency $\omega_{\mathbf{k}}$ is more relevant.

Much of the derivation that follows is an expansion of the discussion in [14],

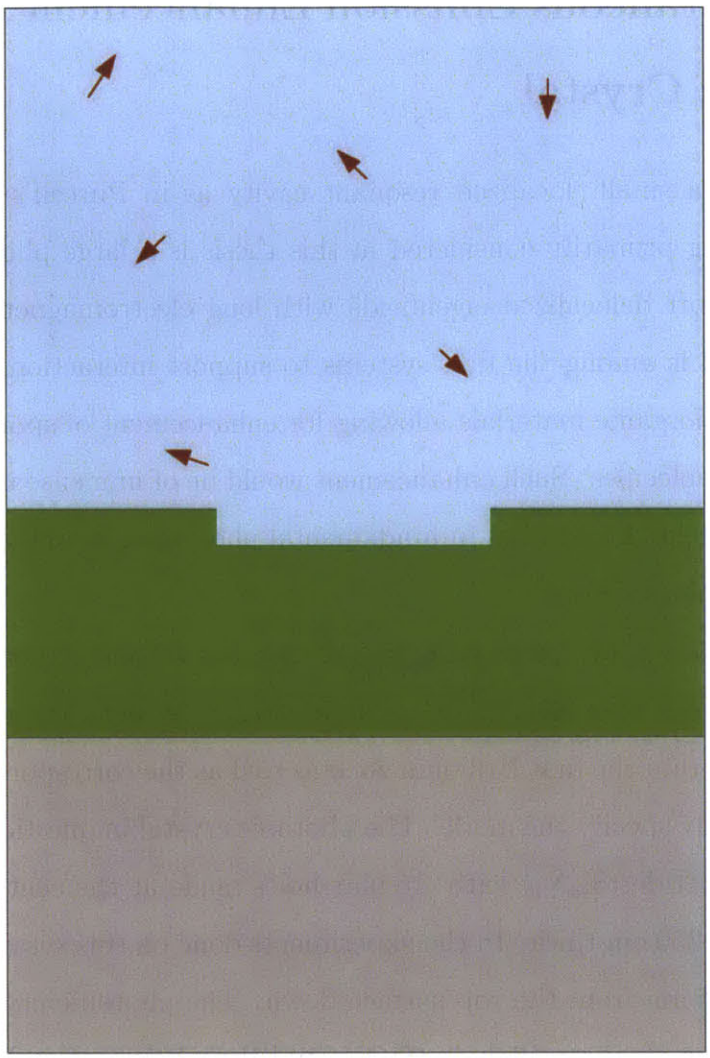

Figure 2-1: 2-dimensional cross-sectional schematic (not to scale) of the photonic crystal studied in [14]: methanol is in light blue, silicon nitride is in green, silicon dioxide is in light gray, and radiating dilute R6G molecules in methanol solution are dark red arrows upon the light blue background

as the semianalytical method and general experimental setup form the basis for the computational analysis of a similar photonic crystal system as discussed in this thesis. Thus motivated, the decay rate of molecules with number density N_0 into a photonic crystal is

$$\Gamma(\omega) = \frac{\pi N_0 \omega |\vec{\mu}_{e,g}|^2}{3\hbar\epsilon_0} \sum_{\mathbf{k},\omega_\mathbf{k}} \int_{\text{gain medium}} \frac{1}{\pi} \frac{\Delta\omega_\mathbf{k}}{(\omega - \omega_\mathbf{k})^2 + (\Delta\omega_\mathbf{k})^2} |\mathbf{E}_{\mathbf{k},\omega_\mathbf{k}}(\mathbf{r})|^2 \, d^3r \qquad (2.13)$$

where $\Delta\omega_\mathbf{k}$ is the half-width at half of the maximum (HWHM) of the mode $(\mathbf{k}, \omega_\mathbf{k})$

(called γ in the previous section), $|\vec{\mu}_{e,g}|^2$ is the square of the norm of the dipole transition matrix element, and SI units with ϵ_0 have been used in this expression as these are more conducive to experimental verification in this instance. For this expression to work, the dipoles are assumed to be homogeneous & isotropic in the solution and are assumed to be randomly polarized (so this decay rate is an average over all polarizations); moreover, this expression is easiest to computationally and experimentally verify when resonances are far apart. As with the small cavity, the decay rate is gotten through a Green's function approach, but rather than expanding the Green's function in eigenfields of the system, it has been expanded instead in normalized Bloch states $\mathbf{E}_{\mathbf{k},\omega_\mathbf{k}}(\mathbf{r})$ which have finite lifetimes given through the quality factor $Q_{\mathbf{k},\omega_\mathbf{k}} = \frac{\omega_\mathbf{k}}{2\Delta\omega_\mathbf{k}}$; this avoids the divergence of the decay rate on resonance when using proper eigenfields which have infinite lifetimes, as was encountered in the previous section. Replacing sums over $\mathbf{k}$ with integrals over $\mathbf{k}$ in the two dimensions parallel to the slab weighted by $\frac{A}{(2\pi)^2}$ in analogy with a solid-state crystal, picking out a particular resonance $(\mathbf{k}, \omega_\mathbf{k})$, setting $\omega = \omega_\mathbf{k}$, and dividing by the total electromagnetic energy to enforce normalization of the Bloch states gives

$$\Gamma(\mathbf{k}, \omega_\mathbf{k}) = \frac{AN_0|\vec{\mu}_{e,g}|^2}{6\pi^2\hbar\epsilon_0}\alpha_{\mathbf{k},\omega_\mathbf{k}}Q_{\mathbf{k},\omega_\mathbf{k}} \tag{2.14}$$

where $Q_{\mathbf{k},\omega_\mathbf{k}} = \frac{\omega_\mathbf{k}}{2\Delta\omega_\mathbf{k}}$ is the total quality factor of the resonance in the photonic crystal and

$$\alpha_{\mathbf{k},\omega_\mathbf{k}} = \frac{\int_{\text{gain medium}} \epsilon(\mathbf{r})|\mathbf{E}_{\mathbf{k},\omega_\mathbf{k}}(\mathbf{r})|^2\, d^3r}{\int_{(\text{all of space})} \epsilon(\mathbf{r}')|\mathbf{E}_{\mathbf{k},\omega_\mathbf{k}}(\mathbf{r}')|^2\, d^3r'} \tag{2.15}$$

is the confinement factor of the electric field energy within the gain medium, which for this system is the methanol/R6G solution.

Meanwhile, the decay rate of these dipoles atop an untextured silicon nitride slab is given by

$$\Gamma_0 = \frac{AN_0^2|\vec{\mu}_{e,g}|^2 n d_{\text{eff}}}{6\pi\hbar\epsilon_0\lambda} \tag{2.16}$$

where $\lambda = \frac{2\pi c}{\omega}$ is the wavelength of the resonance in vacuum, n is the index of refraction of the silicon nitride slab, and d_{eff} is the distance above the slab within

which $1 - \frac{1}{e^2} \approx 86\%$ of the electric field energy remains, as the electromagnetic fields are assumed to be evanescent (exponentially decaying in space) through the lossy gain medium away from the slab. This looks quite similar to the formula $\Gamma_0 = \frac{\omega^3 |\vec{\mu}_{e,g}|^2}{3\pi\epsilon_0 c^3}$ for decay into free space, with a few differences (aside from factors of $2\pi c$ arising from the use of ω versus λ). The first is that the wavelength of the resonance in the silicon nitride slab is different from the wavelength in vacuum by the factor $\frac{1}{n}$. The second is that the decay rate of one dipole needs to be multiplied by the number of dipoles, which is effectively AN_0d_{eff}, where again A is the area of the slab and N_0 is the number density of dipoles, while d_{eff}, in characterizing how lossy the gain medium is, also then characterizes what thickness of dipoles above the slab can actually couple their radiation to the slab for enhancement. The third is that the extra factor of 2 comes from considering only radiation to the region above the slab, because that is where experimental measurements can most easily be made. The fourth is that only one factor of λ is present rather than three as in the case of the small cavity: this can be intuitively understood as a consequence of the periodicity in the plane parallel to the slab, so enhancement will only be seen for observers moving along one dimension, which is the perpendicular axis of the slab.

The enhancement factor is then calculated as

$$\Lambda = 1 + \frac{\Gamma}{\Gamma_0} \frac{Q}{Q_{\text{r,top}}} \tag{2.17}$$

which is the usual general expression multiplied by a factor that accounts for the fraction of photons that decay by radiating only through the top: decay processes include radiating through the top (r,top), radiating through the bottom (r,bottom), or being involved in a nonradiative decay (nr) such as (but not limited to) absorption, so that $\frac{1}{Q} = \frac{1}{Q_{\text{r,top}}} + \frac{1}{Q_{\text{r,bottom}}} + \frac{1}{Q_{\text{nr}}}$. Moreover, the number 1 has been added to the ratio because in addition to enhancing the decay rates of certain modes $(\mathbf{k}, \omega_{\mathbf{k}})$, the photonic crystal can inhibit certain modes altogether. This would mean that those modes are unable to couple to the photonic crystal, so the measured photon emission is purely a result of direct emission into the far-field. In the limit of a very large

volume of methanol/R6G solution sitting atop the photonic crystal, so many more of the dipoles are unable to couple to the slab compared to those dipoles that are able to do so; this leads to the emitted flux becoming identical to that in the situation where the silicon nitride slab is untextured, meaning that the enhancement factor should be unity in such a situation. Plugging in the expressions for Γ and Γ_0 yields

$$\Lambda = 1 + \frac{\lambda\alpha}{\pi n d_{\text{eff}}} \frac{Q^2}{Q_{\text{r,top}}} \tag{2.18}$$

as the enhancement of resonant decay from randomly polarized homogeneous isotropic dipoles atop a photonic crystal slab compared to similar decay from the untextured slab for the same mode. After accounting for the differences in experimental setup and corresponding assumptions, this formula agrees with that in [4].

While this formula is generally true, the fluorescent modes considered in this thesis have $Q_{\text{r}} \propto \frac{1}{k}$, so that the radiative portion of the quality factor diverges at the center of the Brillouin zone, and the total quality factor at that point comes entirely from Q_{nr}. Moreover, from the equation $\frac{1}{Q} = \frac{1}{Q_{\text{r}}} + \frac{1}{Q_{\text{nr}}}$, it can be shown that the quantity $\frac{Q^2}{Q_{\text{r}}}$ is maximized when $Q_{\text{r}} = Q_{\text{nr}}$, which occurs at a specific (usually small) value of k along a particular direction in the Brillouin zone; this is called the Q-matching condition. Hence, when considering a particular mode $(\mathbf{k}, \omega_{\mathbf{k}})$ along a particular direction for $\mathbf{k}$ (so that $\mathbf{k} = k\hat{k}$), Λ starts at 1, increases with k until the Q-matching condition is achieved, and then decreases again as k increases further. It is these modes (that have diverging Q_{r} at the Brillouin zone center and have a definite Q-matching condition producing an increase in the enhancement followed by a decrease as $\mathbf{k}$ increases along a given direction) that are primarily considered in this thesis.

2.3 Random Currents in MEEP

All of the above derivations require quantum mechanics at some level. At the very least, quantum mechanics is needed to describe dipole transitions in an atom as used in Fermi's golden rule. A proper treatment of spontaneous emission would consider

the electromagnetic degrees of freedom to be quantized as well, but this additional requirement can be circumvented by considering a statistical thermodynamic treatment of classical electromagnetic degrees of freedom (as per the Planck density of states in a vacuum). Yet MEEP is unable to simulate even the quantum nature of molecules, let alone the quantum nature of electromagnetic fields. Hence, a different approach is needed. Spontaneous emission can be characterized by classical statistical electromagnetic fields, and the quantum particle nature of light itself is less relevant when considering the enhancement of spontaneous emission by a photonic crystal. Thus, all that should matter is that the electromagnetic fields radiating from molecules in the simulation in MEEP are stochastic, satisfying relations that reproduce the photon density of states for an emitter in a vacuum when the radiating molecule is indeed in a vacuum.

In particular, the response of a dipole density $\mathbf{P}(\mathbf{r},t)$ to a deterministic applied electric field $\mathbf{E}(\mathbf{r},t)$, which is usually written as

$$\frac{\partial^2 \mathbf{P}}{\partial t^2} + \gamma \frac{\partial \mathbf{P}}{\partial t} + \omega_0^2 \mathbf{P} = \sigma \mathbf{E}$$

where ω_0 is the resonant frequency of this oscillator, γ is the finite linewidth of the resonance, and σ is the conductivity, can be modified to read

$$\frac{\partial^2 \mathbf{P}}{\partial t^2} + \gamma \frac{\partial \mathbf{P}}{\partial t} + \omega_0^2 \mathbf{P} = \sigma \mathbf{E} + \mathbf{Q} \tag{2.19}$$

where $\mathbf{Q}(\mathbf{r},t)$ is a stochastic applied field defined at every point in space and time. Much of the discussion that follows parallels that in [5]. Substituting harmonic ($e^{-i\omega t}$) time dependence for each quantity in the previous equation yields

$$\mathbf{P}(\mathbf{r},\omega) = \frac{\sigma \mathbf{E}(\mathbf{r},\omega)}{\omega_0^2 - \omega^2 - i\gamma\omega} + \frac{\mathbf{Q}(\mathbf{r},\omega)}{\omega_0^2 - \omega^2 - i\gamma\omega} \tag{2.20}$$

as the polarization density in terms of the deterministic and stochastic applied fields. As $\mathbf{D} = \mathbf{E} + \mathbf{P}$, then it is convenient to define $\mathbf{X}(\mathbf{r},\omega) = \frac{\mathbf{Q}(\mathbf{r},\omega)}{\omega_0^2 - \omega^2 - i\gamma\omega}$, so that $\nabla \times \mathbf{H} = \frac{1}{c}\left(\mathbf{J} + \frac{\partial \mathbf{D}}{\partial t}\right)$ becomes modified to either $\nabla \times \mathbf{H} = \frac{1}{c}\left(\mathbf{J} + \frac{\partial}{\partial t}\left(\mathbf{D} + \mathbf{X}\right)\right)$ or $\nabla \times \mathbf{H} =$

$\frac{1}{c}\left(\left(\mathbf{J}+\frac{\partial \mathbf{X}}{\partial t}\right)+\frac{\partial \mathbf{D}}{\partial t}\right)$, depending on whether it is more convenient to see $\mathbf{Q}$ as resulting in a stochastic electric flux density as in the former or a stochastic current density as in the latter. The latter interpretation is more relevant for the physics considered in [14] that also underlies this thesis. This is because the stochastic current densities are what correspond to probabilistic quantum dipole transitions in the actively radiating molecules. The only further condition that $\mathbf{Q}$ needs to satisfy, as derived by Rytov [13], is a fluctuation-dissipation relation

$$\langle Q_i(\mathbf{r},\omega)Q_j^\star(\mathbf{r}',\omega')\rangle = b\sigma\gamma\frac{\hbar\omega}{e^{\frac{\hbar\omega}{k_BT}}-1}\delta_{ij}\delta_{(\omega,\omega')}\delta(\mathbf{r}-\mathbf{r}') \tag{2.21}$$

where σ and γ are the parameters from the original deterministic damped driven oscillating dipole density, and b is a constant involving only numerical factors and factors of c depending on the system of units. This is derived from the fluctuation-dissipation relation for $\mathbf{X}$ in conjunction with the permittivity

$$\epsilon(\omega) = 1 + \frac{\sigma}{\omega_0^2 - \omega^2 - i\gamma\omega} \tag{2.22}$$

from the deterministic damped driven oscillating dipole density as well as the Planck density of states from before. MEEP is able to simulate classical stochastic currents that satisfy this autocorrelation function because all the quantum physics lies in the autocorrelation function, so as long as the particle nature of light is unimportant, no further consideration of quantum physics beyond that needs to be present in the simulation. MEEP calls this a *noisy Lorentzian susceptibility*, because the stochastic currents are called as part of a material definition rather than as a source definition; this arises due to the equivalence of $\mathbf{Q}$ contributing to either $\mathbf{J}$ or $\mathbf{D}$, and the constitutive relation $\mathbf{D} = \epsilon\mathbf{E}$ allows for construing $\mathbf{Q}$ as being absorbed as part of the definition of ϵ.

Chapter 3

Comparison of Semianalytical Predictions and FDTD Results

3.1 Photonic Crystal Emission Simulation

One of the main goals of this thesis is to simulate spontaneous emission enhancement from a photonic crystal through a classical FDTD solver like MEEP, as this has been seldom done before. Moreover, validation of these computational methods to simulate spontaneous emission enhancement would allow for further computational developments such as computationally optimizing a structure for spontaneous emission enhancement before experimentally testing it. For this thesis, a very similar system to what has been experimentally tested in [14] is simulated in MEEP. However, there are some key differences to keep in mind.

1. The biggest difference is that the simulations are in 2 dimensions rather than 3; this was done for the sake of time, because 3-dimensional computations are extremely costly in MEEP, yet there is nothing in the formula for spontaneous emission enhancement that depends on the dimensionality of the system. Relatedly, the switch from 3 dimensions to 2 also causes information about the 3-dimensional cylindrical hole shape to be lost in 2 dimensions, as a cylinder when simulated in 2 dimensions along its axis looks like a rectangle; this means

that strictly speaking, if this simulated system were to be reconstructed experimentally, it would look more like a 1-dimensional rectangular grating than a 2-dimensional photonic crystal.

2. In the 2-dimensional case, if the hole is drilled only to a depth of 55.5 nm from the top for consistency with the experiments done on this structure, almost all of the modes with diverging Q_r at the Brillouin zone center are too close to other modes with much smaller finite values of Q_r (i.e. very large linewidths). This difference arises from the above point, which is that information about the hole shape is lost when simulating the 3-dimensional structure in 2 dimensions. This means it will not be possible to see those modes show a increase followed by a decrease in Λ as k increases.

   Initially, it was thought that because the formula for Λ should hold true for any mode, it would be sufficient to simulate modes that have finite Q_r at the Brillouin zone center. However, it was then found that Λ was almost constant over the range of k considered, and the fluctuations in the enhancement calculated from the FDTD method would dwarf any small upward or downward trend in Λ as a function of k, rendering any comparison between simulations and the semianalytical predictions meaningless. Hence, there would have to be a way to produce modes of infinite Q_r at the Brillouin zone center that would be far enough away from modes of finite Q_r that the former modes could be examined by themselves. The only way to rectify this issue has been to make the holes deeper; in fact, in the simulations, the holes are drilled all the way through the slab so that the modes of infinite Q_r at the Brillouin zone center are as far away from other modes as possible.

3. A region of random dipoles can be simulated using the noisy Lorentzian susceptibility in MEEP. However, it is not possible to simulate a statistically homogeneous dilute solution of methanol and R6G in MEEP. Several alternative methods of placing the active dipoles in a relevant region were tried.

   The first method was to place the dipoles in the silicon nitride slab, making

it radiate rather than the methanol. This is because the FDTD code for computing Λ originated from code that was developed to reproduce the results of guided resonances in a photonic crystal slab as detailed in [6]; that code was in fact able to reproduce the results in that paper. However, when using that code to simulate spontaneous emission enhancement for comparison to theoretical predictions and experimental results as has been detailed above, a normalization scheme had to be picked. The first normalization scheme used was a rough heuristic that the average flux from the radiating photonic crystal outside of a resonance should be approximately the flux produced on average by an untextured radiating slab. This was eventually determined to produce unreliable results for the enhancement, as the enhancement was not consistent between different resonances and between different sets of simulations (as multiple simulations of the same structure would be needed to average over the randomness produced by the noisy Lorentzian susceptibility). The second normalization scheme was to simulate the spontaneous emission flux from an untextured radiating slab and divide the flux from a radiating photonic crystal slab by that. However, because in each case the radiating dipoles homogeneously filled the silicon nitride slabs, the normalization calculation had more dipoles than the photonic crystal calculation, as the untextured slab had no methanol hole puncturing it or the dipoles inside the slab in that region.

The second method was to examine the energy density profiles of the desired modes to determine how much passive methanol from the bottom of the hole and above contains 86% (an approximation of $1-\frac{1}{e^2}$, coming from the definition of d_{eff}) of the energy of that mode. This region of methanol would then be made active with a noisy Lorentzian susceptibility. The region was determined to be a cylinder filling the hole up to 65% of its height. There were two problems with this too, though. The first was that by placing the dipoles only within a fraction of the hole, the assumptions of homogeneity and isotropy of the dipoles were broken, so the FDTD enhancement results could no longer be directly compared to the semianalytical predictions. The second was that the normalization could

no longer be done with respect to an untextured slab, because the dipoles were being placed in a region (the hole) that by definition required texturing. Instead, the normalization was taken to be the replacement of the silicon nitride slab with passive methanol, while letting the dipole configuration otherwise remain the same. This too was found to be inconsistent with the semianalytical predictions.

Thus, the closest analogue is to simulate a thin film of active methanol specified with a noisy Lorentzian susceptibility sitting above the passive silicon nitride slab and below a larger volume of passive methanol. To ensure consistency between the photonic crystal emission calculations and the untextured slab emission calculations, the dipole configurations must be identical, so the methanol that fills the hole in the photonic crystal must be passive. The separation of the active and passive methanol regions also means that the notion of d_{eff} is less meaningful. In fact, it should simply be replaced by the thickness d of active methanol simulated. When d is large, most of the active methanol above the slab cannot couple to the slab, and the energy that does couple decays enough through the thick lossy active methanol layer that it will not be seen in the far-field either; there is thus no enhancement of spontaneous emission from the photonic crystal slab as compared to the untextured slab. By contrast, when d is small, almost all of the radiation from the active layer can couple to the photonic crystal slab, so while the absolute magnitudes of flux in the photonic crystal slab case and the untextured slab case will each be small due to the small number of dipoles, the ratio will be quite large. Of course, the lower bound on d due to the resolution of the simulation places an effective upper bound on Λ that can be simulated.

4. As a final minor point, the finite extent of the computational cell means that it is not possible to normalize the electric field energy in the gain medium to the electric field energy in all of space when calculating the confinement factor α. The expression

$$\alpha = \frac{\int_{\text{gain medium}} \epsilon(\mathbf{r})|\mathbf{E}(\mathbf{r})|^2 \, d^3r}{\int_{\text{full computational cell}} \epsilon(\mathbf{r}')|\mathbf{E}(\mathbf{r}')|^2 \, d^3r'} \tag{3.1}$$

is used instead.

These are the changes that must be made for the simulation to work correctly. There is one other change that is done for convenience. The simulations are unburdened by the inability of experimentalists to measure the spontaneous emission below the slab, as flux planes can be placed anywhere in the computational cell. Therefore, the total spontaneous emission flux is considered rather than only emission above the slab, where the latter case is considered in [14]. This means that $Q_{\mathrm{r,top}}$ can be replaced by Q_{r} to account for all of the spontaneous emission flux from the photonic crystal slab. Additionally, it is assumed in the derivation of enhancement factor in the previous chapter that the spontaneous emission from the untextured slab is sent equally above and below the slab. To fix this and thereby account for the spontaneous emission flux from both sides, the decay rate for the untextured slab simply needs to be doubled. Hence, given the conditions above,

$$\Lambda = 1 + \frac{\lambda\alpha}{2\pi n d}\frac{Q^2}{Q_{\mathrm{r}}} \tag{3.2}$$

is the enhancement factor that should be seen in simulations for a given mode (k, ω_k), where again n is the index of refraction of the silicon nitride making up the slab. Note that the value of λ in nanometers is given by the ratio of the length scale a in nanometers to the numerical value of ω in MEEP, as $\lambda = \frac{2\pi c}{\omega}$, and ω in inverse seconds is given by the MEEP value multiplied by $\frac{2\pi c}{a}$. In these simulations, the length scale is chosen to be $a = 321.4\,\mathrm{nm}$. A schematic of the photonic crystal system simulated can be seen in figure 3-1. The silicon nitride slab is simulated by a passive nondispersive slab of index $n = 2.018$, the silicon dioxide substrate is simulated by a passive nondispersive block of index $n = 1.45$, the passive methanol is simulated by passive shapes of index $n = 1.33$, and the active layer is simulated with base index $n = 1.33$, with the other details to follow.

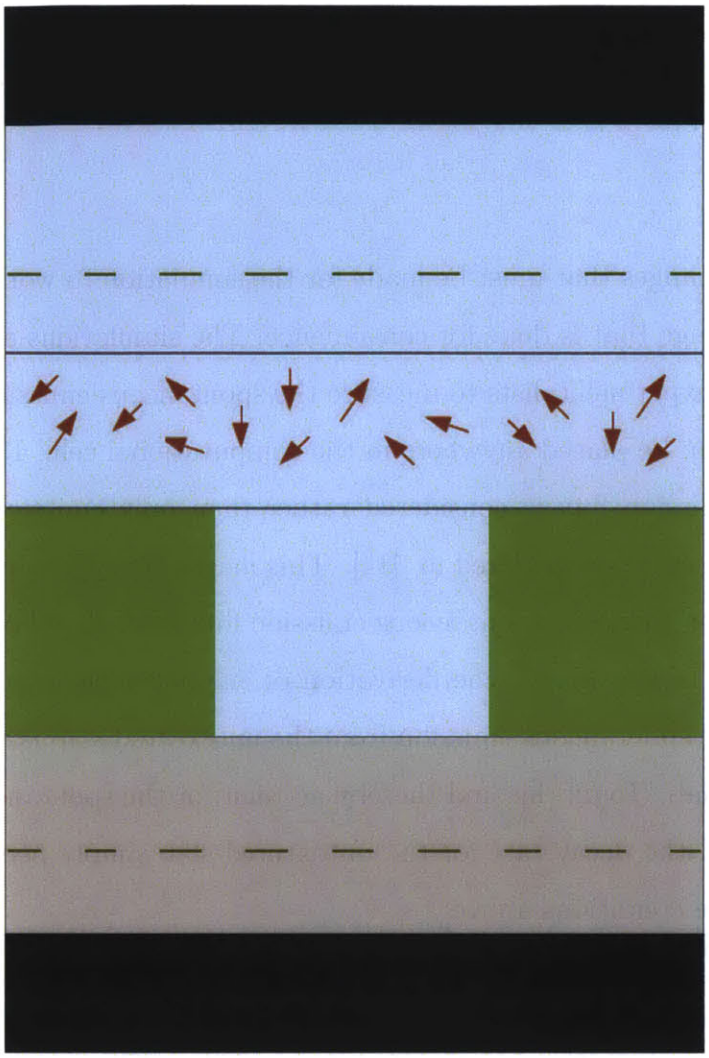

Figure 3-1: Schematic (not to scale) of the photonic crystal simulated in MEEP in 2 dimensions: passive methanol is in light blue above and below the dark gray solid lines, silicon nitride is in green, silicon dioxide is in light gray, and the active methanol film is enclosed between two dark gray solid lines as dark red arrows on a light blue background; dark yellow broken lines denote the two flux planes for computing fluxes, and black on each end is the PML boundary

3.2 Finding Modes

Because spontaneous emission enhancement for photonic crystal resonant modes is being analyzed, the first thing that should be done is to find the resonant modes. This is done by performing the Harminv algorithm, as described further in Appendix A, with a single broadband Gaussian dipole source: usually, this is done with a central frequency of 0.6 and a frequency width of 0.8 in MEEP units. The command

"run-k-points" can be used to find modes through the Harminv algorithm for several different values of k at a time. Because the photonic crystal is oriented parallel to the yz-plane, only k_y and k_z are meaningful for enforcing periodic boundary conditions, and because the simulation is done in 2 dimensions, only k_y remains. Henceforth, k_y and k are synonymous, with the latter used for the sake of brevity (except in cases where more clarity is required). Typically, k would be varied to be not more than $0.02 \times \frac{2\pi}{a}$ where the correspondence between angle off of normal incidence to k is given approximately by $\frac{\theta}{1^\circ} \approx \frac{100ka}{2\pi}$ for small k. This upper bound was chosen because the boundaries at the extremes of the x-axis are made of PML: computations with PML start to fail for higher angles (compared to 2°) off of normal incidence unless the PML is made extremely thick, which would then make the computations extremely costly.

Once the modes are found for each k for a broadband Harminv computation, the ones that have diverging Q_r at $k = 0$ are selected as desirable for the FDTD flux computation. This is contingent on those modes being far away in frequency from any other modes seen for all 3 possible current polarizations. Because these computations are in 2 dimensions in the xy-plane, there is a splitting between TE and TM fields. The TE fields E_x, E_y, and H_z may arise from electric current sources along x or y, while the TM fields H_x, H_y, and E_z may arise from electric current sources along z. (Magnetic current sources are not considered here because the experiment in [14] with which these simulations are to be verified uses electric rather than magnetic dipoles for producing spontaneous emission.)

The Harminv process for multiple k values is done twice for each current polarization. The first time is for when the thin methanol film between the slab and the thick methanol bulk is also made to be passive and nondispersive. The results of this calculation are the resonance frequencies and the corresponding radiative lifetimes Q_r for each k; the output is Q_r rather than Q because there is no absorption or other nonradiative decay mechanism when the methanol film and all other dielectric components are passive and nondispersive. The second time is for when the thin methanol film is made to be dispersive and slightly lossy, which in this case is a Lorentzian susceptibility with no noise. There is no noise because there should not be more

dipoles present than the original single Gaussian source when finding resonant modes for the photonic crystal, yet the dispersion and loss seen when the film is active should be accounted for as well (which is why the thin methanol film remains a non-noisy Lorentzian susceptibility for this particular calculation). Here, the results should yield essentially the same resonance frequencies as before, but the quality factors Q are lower because they include both radiative and nonradiative decay mechanisms. These values of Q and Q_r are plugged into the equation for the spontaneous emission enhancement, along with $n = 2.018$ for the silicon nitride slab, $d = 100\,\text{nm}$ for the thin methanol film, $\lambda = \frac{a}{\omega_{\text{MEEP}}}$ where $\omega_{\text{MEEP}} = \frac{a\omega}{2\pi c}$ with $a = 321.4\,\text{nm}$, and α as described below.

For computing α, one more Harminv computation needs to be performed. Rather than inputting a broadband source, a narrow-band source with the central frequency equal to the resonance frequency ω_k and with a corresponding frequency width of $\frac{6\omega_k}{Q_k}$ is excited. Moreover, because confinement in the gain medium can only occur when it is lossy, the Harminv computation is done when the thin methanol film has a (non-noisy) Lorentzian susceptibility. The output is a set of HDF5 files, each of which is a matrix containing values for a quantity of interest evaluated at each pixel in the simulation. The quantity of interest here is the electric energy density $\epsilon|\mathbf{E}|^2$. The integral of the electric energy density over the gain medium is discretized as a sum over all pixels in the thin methanol film, and the integral over all space is discretized as a sum over all pixels in the computational cell. The ratio of these sums is thus α. Because α is approximated to be constant over the range of k, this Harminv computation only needs to be performed for one of the desired modes at a single value of k. It was found for these computations that on average for the desired modes, $\alpha \approx 0.046$, with the approximation being exact at $k = 0.006 \times \frac{2\pi}{a}$, and with deviations in α from this constant value being less than 2% over the range of k considered. In figure 3-2, contour plot of an example energy density at $k = 0.006 \times \frac{2\pi}{a}$ is shown below the contour plot of the dielectric structure that MEEP simulates. Note how this and other modes largely confine the energy density to the photonic crystal slab. Also note that the smoother variation in the dielectric function across space

despite the discretization across the lattice arises from subpixel averaging.

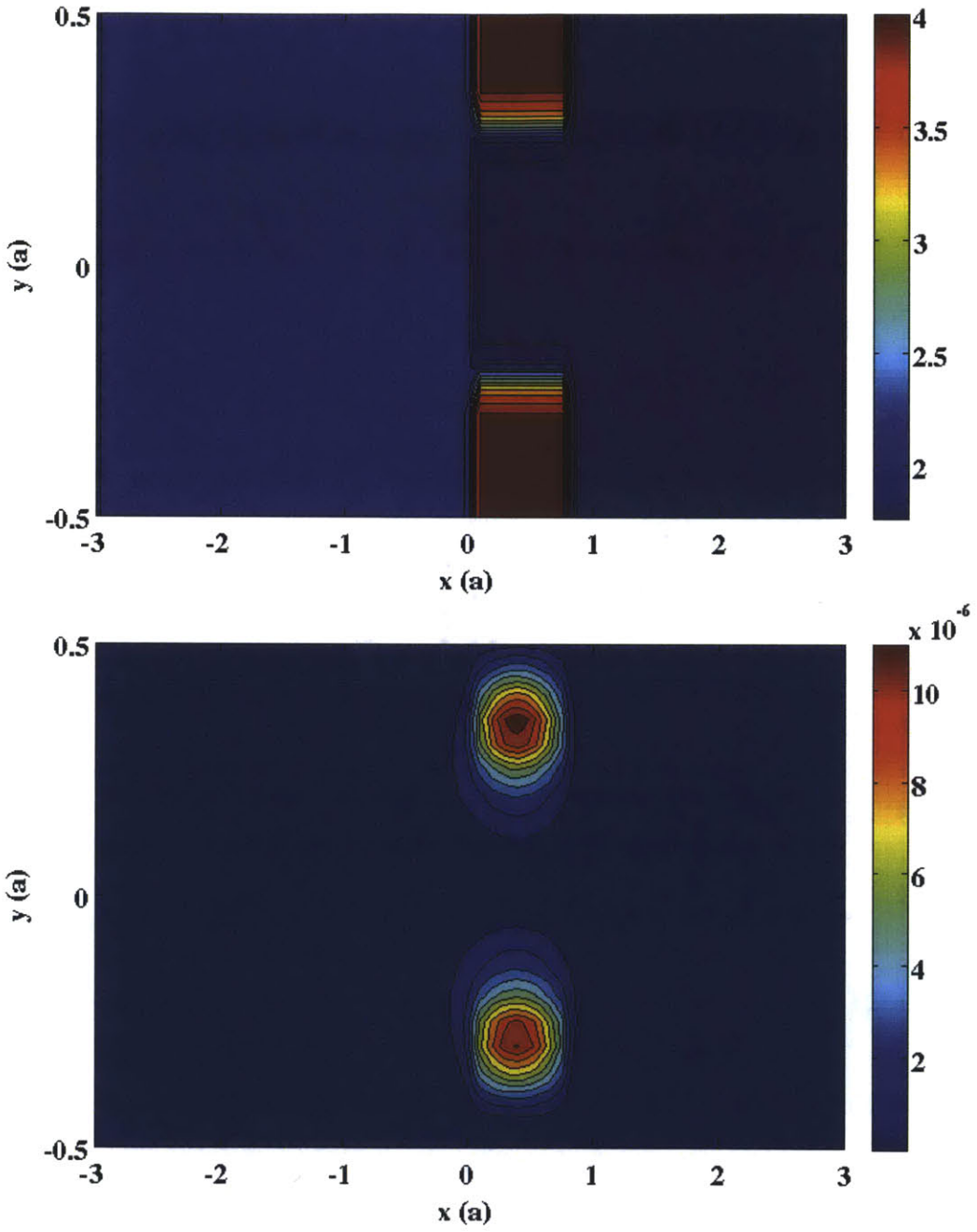

Figure 3-2: Above: contour plot of ϵ (relative dielectric) as a function of position, as simulated in MEEP with subpixel averaging; below: contour plot of the electric field energy (arbitrary units) as a function of position for $k = 0.006 \times \frac{2\pi}{a}$, showing large confinement of the mode within the silicon nitride slab

The modes that were found to be have infinite Q_r at the Brillouin zone center and

were farthest from other modes for current excitations along any direction were those modes with a resonant frequency between $0.6111 \times \frac{2\pi c}{a}$ and $0.6136 \times \frac{2\pi c}{a}$ (corresponding to wavelengths between 523.8 nm and 525.9 nm), where the small decrease in ω occurs gradually as k is increased. These modes are excited by currents along the z-axis only; this means that only the TM fields are resonant, while the TE fields are not. These were the modes considered for FDTD flux computations.

3.3 Computing Emitted Flux

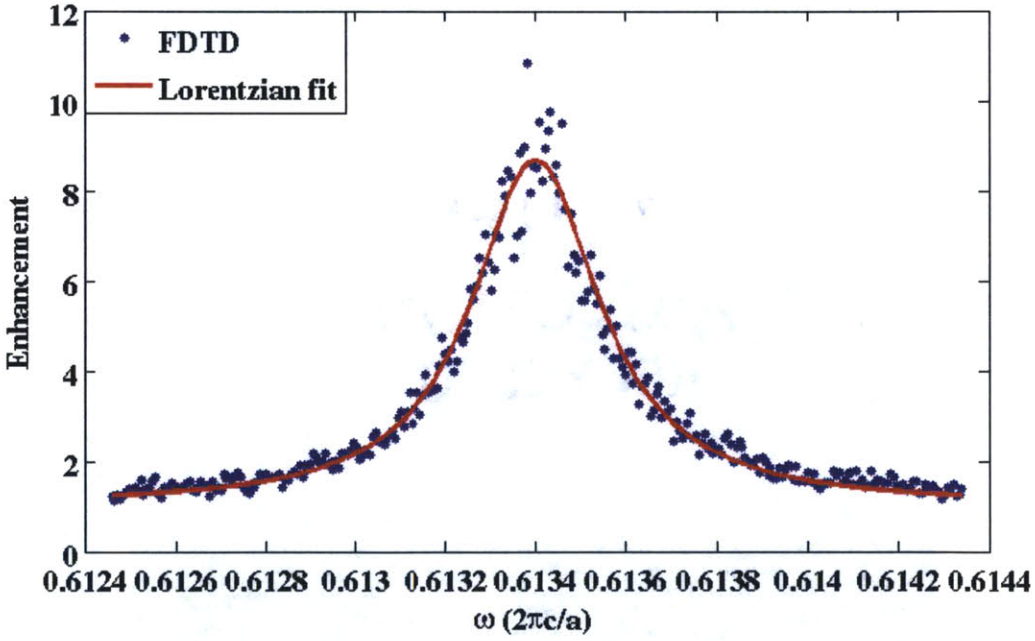

Figure 3-3: Enhancement spectrum of the desired resonance around $k = 0.006 \times \frac{2\pi}{a}$, with the FDTD results as blue dots and the Lorentzian fit as a red line

Once the modes are found and α is calculated for each desired mode, the FDTD flux calculations can be performed. For the sake of time, only a single band (far away in frequency from other bands at each k and for each current polarization) with diverging Q_{r} at $k = 0$ was considered. The thin methanol film was made active as a noisy Lorentzian susceptibility with the same loss parameters as the Lorentzian susceptibility used with Harminv, and the active dipoles are excited at a narrow band (of

width $\frac{6\omega_k}{Q_{k,\omega_k}}$) centered around the chosen resonance frequency ω_k. The full code used is detailed in Appendix A. The system setup is otherwise largely the same as in the Harminv calculations. Because the active medium is characterized by random noise, the emitted flux is only meaningful after an ensemble average; it was determined that averaging over 100 calculations is sufficient for the average emitted flux to converge. For the particular mode for each k, a set of 100 calculations is performed for the photonic crystal slab, and a set of 100 calculations is performed for the untextured slab. Then, for each k, each set of 100 is averaged, and then the resulting average photonic crystal slab flux is divided by the average untextured slab flux to yield the enhancement as a function of frequency. This enhancement spectrum typically looks like a Lorentzian as is theoretically predicted, but there is some amount of noise in the enhancement spectrum, so the comparison is not exact. These discrepancies can be overcome by nonlinearly fitting the FDTD-computed enhancement spectrum to a Lorentzian function (with a baseline vertical shift of 1), and the peak of that fit is taken to be the FDTD-calculated enhancement for that value of k. An example enhancement spectrum is shown in figure 3-3 for $k = 0.006 \times \frac{2\pi}{a}$, with the FDTD results shown as blue dots and the nonlinear Lorentzian fit shown as a red line. Note how compared to the Lorentzian fit, the FDTD enhancement appears to fluctuate almost randomly with small amplitude from one frequency to the next. This is to be expected because the time given for collecting the flux from random dipoles at each frequency is large enough for convergence in the flux results for this mode.

3.4 Comparing to Semianalytical Results

Seen in figure 3-4 is a comparison between the enhancement as calculated by semi-analytical methods, shown as a red line, and FDTD computations, shown as blue dots. The relative difference between the two sets of results varies between 0.4% and 6.9%, and on average the relative difference is 3.4%. As expected, the enhancement as calculated from the semianalytical model starts from 1 at $k = 0$ and shows an upward trend followed by a downward trend as k increases, as is characteristic of a mode of

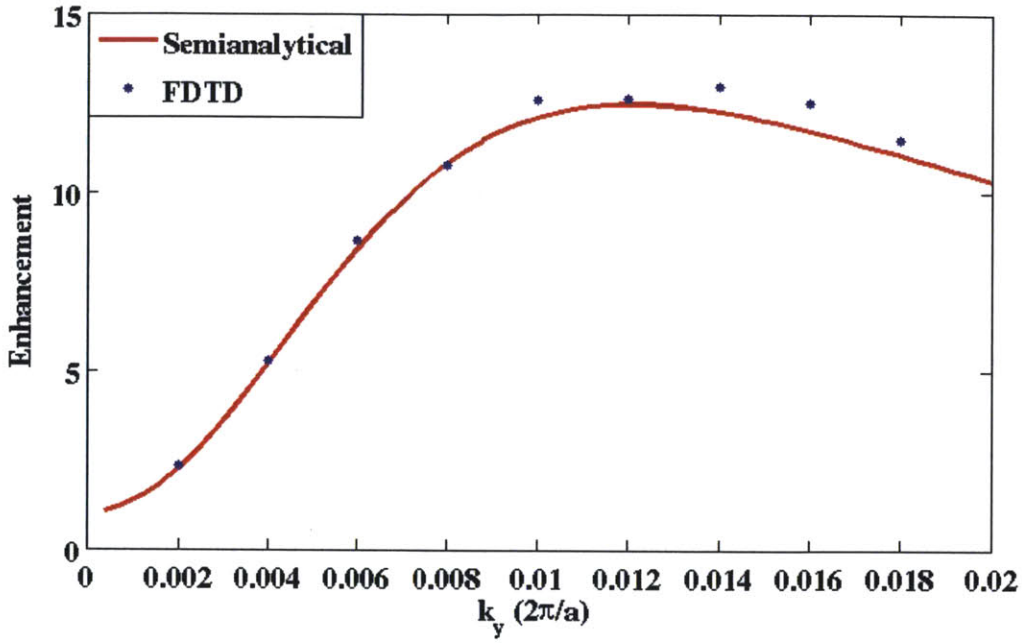

Figure 3-4: Comparison of the enhancement of the desired mode at each k between semianalytical predictions (red curve) and FDTD computations (blue dots)

infinite Q_r at the Brillouin zone center; the enhancement calculated from the FDTD computations almost exactly follows this trend as well. Hence, this method of using classical stochastic currents in an FDTD electromagnetic solver to simulate random emission (even when the source of the randomness is actually quantum mechanical in nature, as in spontaneous emission) is effective.

3.5 Half-Sphere System

In most nanophotonic systems, a semianalytical model cannot be created to describe spontaneous emission from such a system; the photonic crystal system described above is an exception rather than the rule. In the majority of cases, then, it would be useful for experimentalists to have an idea of what features might be seen in spontaneous emission in a nanophotonic system before conducting the experiment, and the only other way to know in advance is to perform simulations through computational electromagnetic solvers such as MEEP.

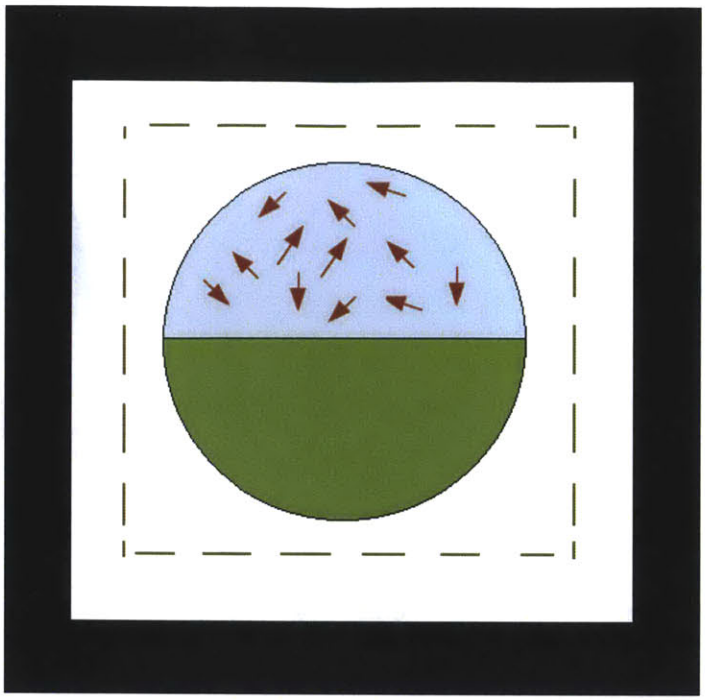

Figure 3-5: 2-dimensional cross-sectional schematic (not to scale) of the half-sphere system simulated in MEEP in 3 dimensions: active "silicon nitride" of $n = 2.018$ is the dark red arrows on the light blue background, passive "metal" of $n = 100$ is in green, and vacuum is in white; dark yellow broken lines denote the flux planes for computing fluxes (of which there are 10 in 3 dimensions), and black surrounding the system is the PML boundary

In this section, a system called the "half-sphere" system is discussed. This system could be encountered experimentally if a spherical nanoparticle is partially implanted in tissue and the half that is visible outside the tissue can fluoresce, while the half that is embedded in the tissue is made of a metallic substance. A schematic of this system is seen in figure 3-5. A metal is expected to reflect light in large ranges of wavelengths, so if the fluorescing half is called the top and the passive metallic half is called the bottom, it would be reasonable to expect that the emitted flux spectrum will be more biased in the direction of the top than the bottom, compared to a sphere that uniformly fluoresces.

Such a system can be simulated in MEEP in a similar way to the photonic crystal system above. Here, instead of periodic boundary conditions, the boundaries of the computational cell are fully covered with PML, as this sphere is taken to be isolated.

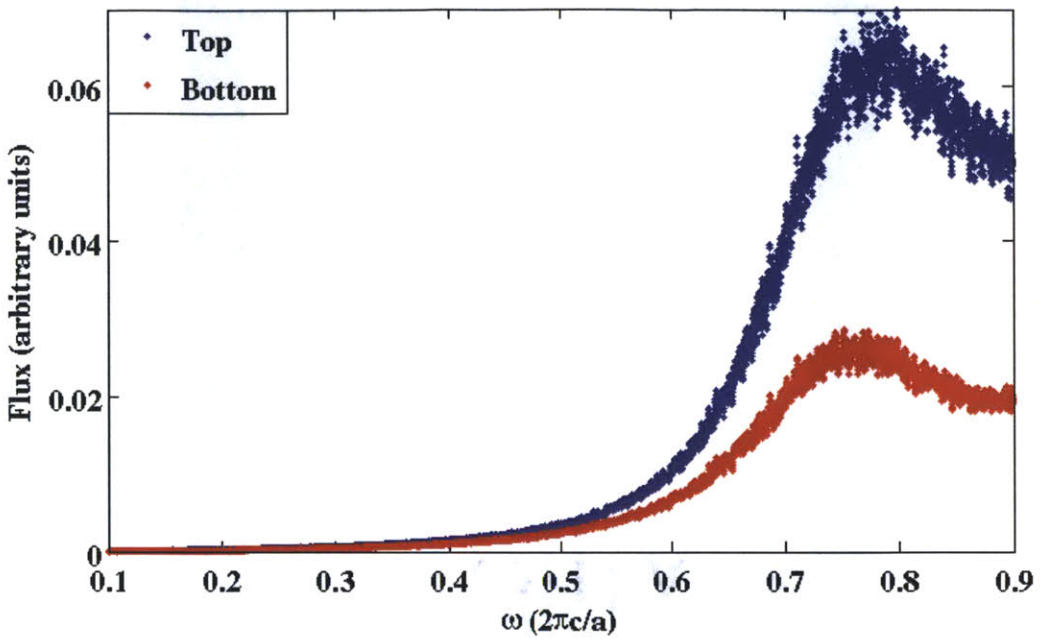

Figure 3-6: Comparison of flux spectra above (blue dots) versus below (red dots) the half-sphere system

The sphere was set to have a radius of $0.2a$. The active top half was taken to be radiating "silicon nitride"[1] of base index $n = 2.018$, and this was again simulated with a noisy Lorentzian susceptibility. That said, MEEP was unable to simulate the passive metallic bottom half with the dispersive lossy dielectric function of an actual metal like gold. Instead, the bottom half was taken to be a passive nondispersive dielectric of index $n = 100$. This is still acceptable because the large index contrast between the bottom half and the top half (and the vacuum surroundings too) means that despite the lack of direct reflection due to the absence of skin depth, most light that enters the bottom will be totally internally reflected and come out of the top anyway. Moreover, the index contrast between the bottom and the surrounding vacuum is larger than the index contrast between the bottom and the top, so more internal reflection will occur at the former boundary than at the latter. Index contrasts creating a bias in the direction of flux emission were seen even in the photonic crystal system, where the slab has index $n = 2.018$, the substrate has index $n = 1.45$, and the methanol above

[1]Quotes around the material names are indicative that this system has not been experimentally studied as of yet, so the only relevant information to be considered for simulation is the index n.

has index $n = 1.33$. There, howeer, the largest index ratio is approximately 1.5, so the difference in the emitted flux to the top versus the bottom from equidirectional emission was very small; anyway, in that case, the information about differences in directionality were erased by considering only the enhancement of total emission (in both directions) above the photonic crystal slab over total emission above the untextured slab. In this system, by contrast, the quantity of interest is in fact the difference in directional emission, and the difference is generally amplified due to the much larger index contrast between the bottom hemisphere and the top hemisphere as well as the surrounding vacuum.

Five rectangular flux planes surrounded the top hemisphere and another five surrounded the bottom, with the total from each respective set of five flux planes taken to be the top or bottom flux spectrum. The results are shown in figure 3-6, where the spectrum for the top is shown as blue dots and the spectrum for the bottom is shown as red dots. For every frequency, on average, the flux from the top is about 2.5 times the flux from the bottom. As only a rough comparison was desired, no further attempt was performed to make this more rigorous, and the time for the flux planes to collect data was not further checked to ensure convergence (though the apparent random fluctuations in the spectrum from one frequency to the next is likely indicative of convergence).

3.6 Future Investigations

The success of the FDTD computational method in reproducing the semianalytical predictions of spontaneous emission enhancement by a photonic crystal, combined with the separate validation of those semianalytical predictions by experiment, lends the computational method to further use in suggesting future experimental directions. In particular, the spontaneous emission enhancement by a photonic crystal being intimately tied to the spectral density of states suggests that the spontaneous emission enhancement can be nonlinearly optimized by appropriately modifying the photonic crystal structure. From solid-state physics, the density of states as a function of ω is

related to the derivative of $\mathbf{k}$ with respect to the ω in a given band, so when ω varies very slowly with $\mathbf{k}$, it would be reasonable to expect that the density of states becomes very large for that value of ω. It would then be interesting to see if a photonic crystal that is computationally optimized specifically for spontaneous emission enhancement is the same structure as the photonic crystal optimized to produce a flat band over a large range of $\mathbf{k}$ in one or more directions in the Brillouin zone.

The FDTD computational method when applied to the half-sphere system needs to be more rigorously checked for convergence in both the flux collection time and the number of averages performed. Once that is done, it would be interesting study one (or two) other systems. Another system to consider would be one that replaces the passive nondispersive high-index "metal" with a material that has dielectric resonances in the visible regime, as these dielectric resonances may produce new behavior in the flux spectra of interest. A third system would be to consider an alternative method of reflecting electromagnetic emission preferentially in one direction: instead of creating a sphere where the low-index top hemisphere radiates and the entirety of the bottom hemisphere is a passive metal, the entire sphere could be a radiating low-index material, but the exterior of its bottom hemisphere could be coated with a thin metal layer.

Chapter 4

Nanoparticle Scatterers of Infrared Light

4.1 General Quasistatic Structures

The second part of this thesis considers the absorption and scattering of infrared light by metallic nanoparticles. Not as much work has been done in characterizing nanoparticles that efficiently scatter and absorb infrared light as has been done in the visible regime, so it would be useful from the standpoint of basic physics to examine what differences arise. Moreover, if nanoparticles can be designed to efficiently scatter and absorb infrared light, these properties can be used for medical and military applications, such as tissue imaging through scattering, tumor destruction through absorption, or obscurance through absorption and scattering.

When light is incident on a dielectric or metal particle, the particle is said to be quasistatic when its size is significantly smaller than the wavelength of the incident light. This is because the particle is small enough that the spatial variation of the incident electromagnetic fields over the range of the particle can be neglected, and only the time variation needs to be considered. In general, light incident on a particle can be absorbed or scattered, and the cross sections C of absorption or scattering, each of which is respectively the absorbed or scattered power divided by the intensity of the incident electromagnetic field, can be added to yield the extinction cross section

$C_{\text{ext}} = C_{\text{abs}} + C_{\text{sca}}$; this extinction cross section is a measure of how effective the particle is at inhibiting coherent transmission of the incident light. Often, a more useful metric of this inhibition is the extinction cross section per unit volume $\frac{C_{\text{ext}}}{V}$, as this allows for comparison of the performance of particles of many different sizes for a given wavelength of incident light; for light incident on a single particle, this is just the extinction cross section of that particle divided by its volume.

As per [10], for certain values of (complex, frequency-dependent) ϵ, a quasistatic particle can have a self-sustaining surface charge distribution even without an incident electromagnetic field. If light of a wavelength that excites one of these resonant values of ϵ is incident on the particle, the resonant surface charge distribution will then maximize $\frac{C_{\text{ext}}}{V}$. The angle-averaged extinction cross section per unit volume is

$$\frac{C_{\text{ext}}}{V} = \frac{2\pi}{3\lambda} \sum_n \text{Im}\left(\frac{1}{L_n - \xi(\omega)}\right) p_n \tag{4.1}$$

for any vacuum wavelength λ of incident light. Here, the index n labels the different resonant surface charge distribution, p_n is related to (but not exactly) the dipole moment of that charge distribution, L_n is the depolarization factor of that charge distribution which describes how an electric field incident on a particle is partially canceled by its polarizability and its free charges, and $\xi(\omega) = -\frac{1}{\chi(\omega)}$ where the (complex) electric susceptibility $\chi(\omega) = \epsilon(\omega) - 1$. Resonant extinction occurs when the frequency ω is such that $L_n = \xi_{\text{r}}(\omega)$, where the subscripts r and i denote the real and imaginary parts, respectively, of a complex number.

The depolarization factor L_n is generally known for common particle shapes, but bounds can still be placed on the extinction cross section per unit volume only knowing the material properties and incident wavelength (without knowing the particle shape). In particular, as the materials considered here are metallic with $0 < -\frac{\chi_{\text{r}}}{|\chi|^2} < \frac{1}{3}$ in the relevant frequency range, the shape-independent upper bound on the resonant extinction cross section per unit volume is

$$\frac{C_{\text{ext}}}{V} \leq \frac{2\pi}{3\lambda} \frac{2\chi_{\text{r}}^3(1+\chi_{\text{r}}) + \chi_{\text{i}}^2(3 + 2\chi_{\text{r}} + 4\chi_{\text{r}}^2) + 2\chi_{\text{i}}^4}{\chi_{\text{i}}(\chi_{\text{i}}^2 + (1+\chi_{\text{r}})^2)} \tag{4.2}$$

where the dependence on ω has been suppressed for brevity. This equation remains true for general quasistatic particle shapes in both the visible and infrared regimes, and may remain true even outside of those regimes as well.

4.2 Infrared Half-Wavelength Structures

From basic antenna theory, a dipole antenna whose total length is half of a wavelength of the desired electromagnetic radiation maximizes radiated power by virtue of maximizing the voltage difference between the ends of the antenna, thereby maximizing the current amplitude as well. Similar considerations may hold for metal structures absorbing or scattering incident light. Given this, an extensive study of ellipsoidal metal particles with sizes around a quarter or half of a wavelength (i.e. not quasistatic) of incident infrared light has been performed in [2], using FDTD computational tools. The ellipsoidal structures were extremely prolate (rods) or oblate (disks). The dimensions of the ellipsoids, conductivity, incident wavelength, and orientation angles were all varied to yield extinction cross sections per unit volume as well as other scattering and absorption quantities of interest.

The study in [2] uses the Drude model

$$\epsilon(\omega) = 1 - \frac{\sigma_0}{\epsilon_0 \omega(\omega\tau + i)} \tag{4.3}$$

where $i = \sqrt{-1}$, σ_0 is the zero-frequency conductivity, τ is the relaxation time of free electrons in the metal, and ϵ_0 is the permittivity of free space (depending on units). Furthermore, when one of the dimensions of the ellipsoid becomes smaller than 100 nm, an empirical correction by the aspect ratio is required, given by

$$\sigma_0 \to \frac{h}{1+h}\sigma_0 \tag{4.4}$$

where h is the aspect ratio, which is $\frac{D}{l}$ for a rod ellipsoid of equatorial diameter D and axial length $l > D$, or $\frac{T}{D}$ for a disk ellipsoid of axial thickness T and equatorial diameter $D > T$. That study found that making rods and disks out of aluminum,

which has $\sigma_0 = 2.81 \times 10^7 \frac{\text{S}}{\text{m}}$ and $\tau = 8.88 \times 10^{-15}\,\text{s}$, optimizes the angle-averaged $\frac{C_{\text{ext}}}{V}$ for unpolarized light of $\lambda = 10\,\mu\text{m}$. In particular, the optimal structures generally have at least one dimension close to half of the wavelength of the incident light. One particular figure of merit for comparison[1] is that a rod of length $4.8\,\mu\text{m}$ and equatorial diameter $0.1\,\mu\text{m}$ has $\frac{C_{\text{ext}}}{V} \approx 22\,(\mu\text{m})^{-1}$ for unpolarized incident light of $\lambda = 10\,\mu\text{m}$.

4.3 Quasistatic Structures in the Infrared Regime

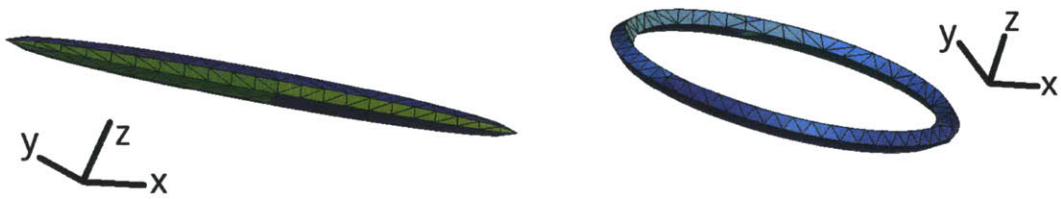

Figure 4-1: Example meshes of quasistatic structures considered, including a rod (left) of length 2400 nm & equatorial diameter 92 nm, and a torus (right) of major radius 36 nm and minor radius 2.5 nm

The structures extinguishing infrared light studied in this thesis, by contrast to [2], were structures that were either smaller than half of a wavelength or were quasistatic structures compared to infrared light of $\lambda = 10\,\mu\text{m}$. Two main types of structures considered were (prolate) rod ellipsoids as well as tori, for which example meshes are shown in figure 4-1. If the equatorial radius of the rod is small enough compared to its long radius (which itself is small compared to the wavelength of light considered), then such a rod that has an alternating current applied to it would behave very much like a Hertzian electric dipole antenna. By contrast, a small torus of a comparable size to a Hertzian dipole antenna has a reduced dipole moment compared to the Hertzian dipole antenna, so if the applied current is the same as in the case of the

[1] Unfortunately, simulations in SCUFF-EM were unable to exactly reproduce the results from this existing study, though general trends in the extinction cross section per unit volume were easily reproducible. Simulations in SCUFF-EM were able to reproduce well-known analytical and numerical results for both dielectric and metal spheres, so it is unclear what other information may have been needed from the existing study for simulations in SCUFF-EM to better reproduce those results. The figure of merit quoted is a recalculation using SCUFF-EM, not the number listed in that paper.

rod, the radiated power should be less for a loop; tori only perform comparably to rods at the scale of half of a wavelength. Likewise, a quasistatic torus with an alternating current applied to it would behave very much like a small magnetic dipole antenna. Given this, it is reasonable to presume that thin rod ellipsoids will be very effective at absorbing and scattering infrared light too, while tori will be comparatively less effective. That said, because extinction mechanisms behave rather differently in the quasistatic regime compared to the half-wavelength regime, there may strictly speaking be no reason to believe a priori that one type of structure will perform better than the other.

The particular structures considered were rods and tori made of either aluminum or silver. The code to do this is outlined in Appendix B. In each case, because the structures had at least one dimension that was not larger than 100 nm, the correction from equation 4.4 was used; for rods of length l and equatorial diameter D, $h = \frac{D}{l}$, while for tori of minor radius r and major radius R, $h = \frac{r}{\pi R}$, as the torus has been approximated to be a rod of equatorial diameter $2r$ and length $2\pi R$ bent into a circle. Each torus was optimized for infrared extinction over the major radius R in the region of $0.5 - 4\,\mu$m keeping the minor radius r fixed at 50 nm, or over the major radius R in the region of $10 - 50$ nm keeping the minor radius r fixed at 2.5 nm. Likewise, each rod was optimized over the length l in the region of $1 - 8\,\mu$m keeping the equatorial diameter D fixed at 100 nm, or over the length l in the region of $80 - 300$ nm keeping the equatorial diameter D fixed at 5 nm. Additionally, the aluminum rod only was separately optimized over the equatorial diameter D in the region of $40 - 120$ nm keeping the length l fixed at $2.4\,\mu$m for comparison with results from [2]. The optimization results are shown in figures 4-2, 4-3, 4-4, 4-5, & 4-6, and the optimal results have been further compiled into table 4.1 for rods and table 4.2 for tori.

There are a few things that can be noted right away from the tables. The first is that for each pair of material and shape, the optimal $\frac{C_{\text{ext}}}{V}$ is essentially unchanging (where the tiny differences in those values may just be because of slight computational differences such as different meshes), and the corresponding aspect ratio h remains in a reasonably close neighborhood for each such pair. The second is that aluminum

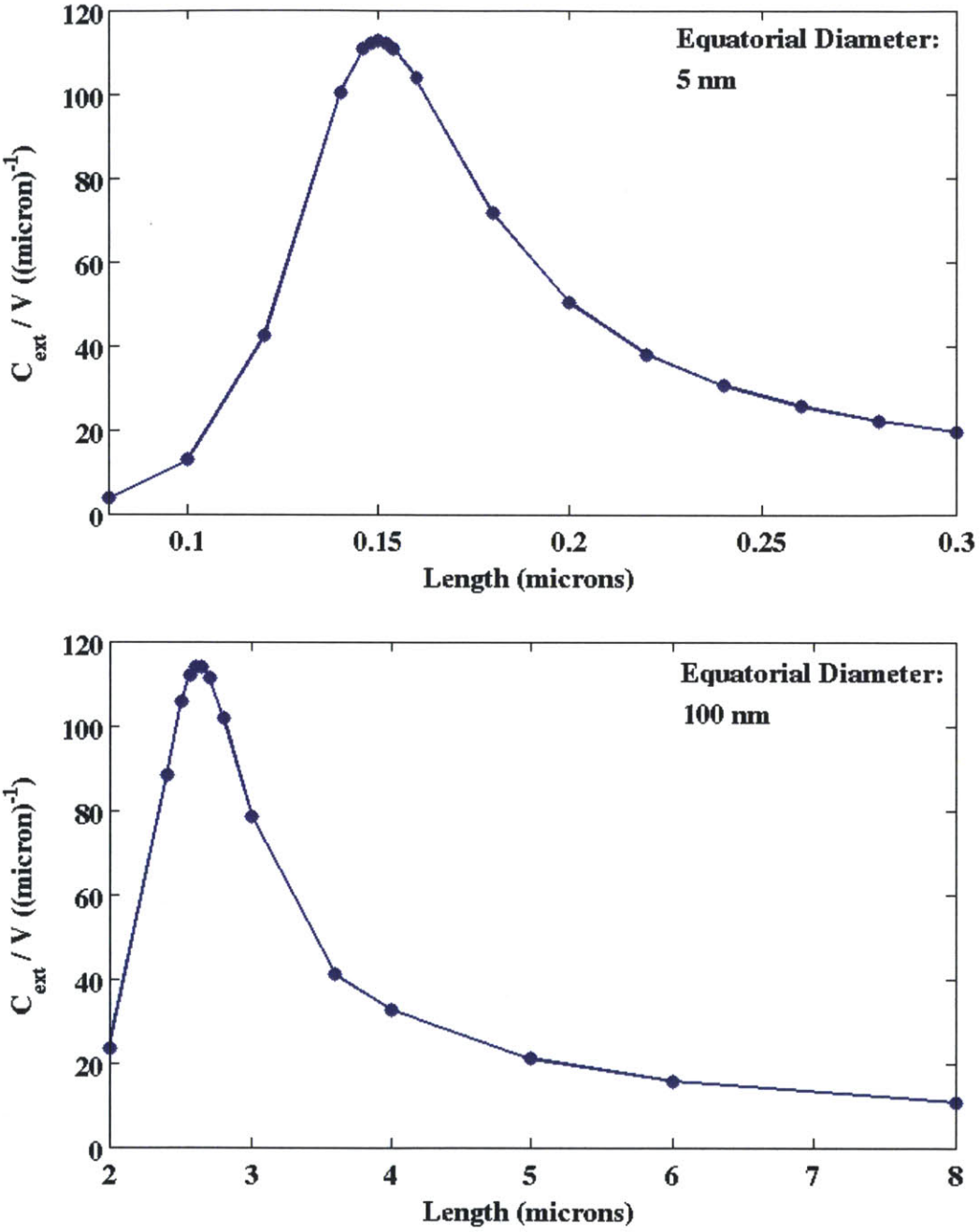

Figure 4-2: $\frac{C_{ext}}{V}$ optimization sweeps of aluminum rods over length with the equatorial diameter fixed; top: equatorial diameter is 5 nm; equatorial diameter is 100 nm; note that lines are merely to guide the eye and are not indicative of fitting or interpolation

outperforms silver for each shape, matching results from [2]. The third is that, as expected, the tori perform worse than rods when the dimensions are smaller than half of a wavelength. The fourth is that the optimal aluminum rods handily outperform

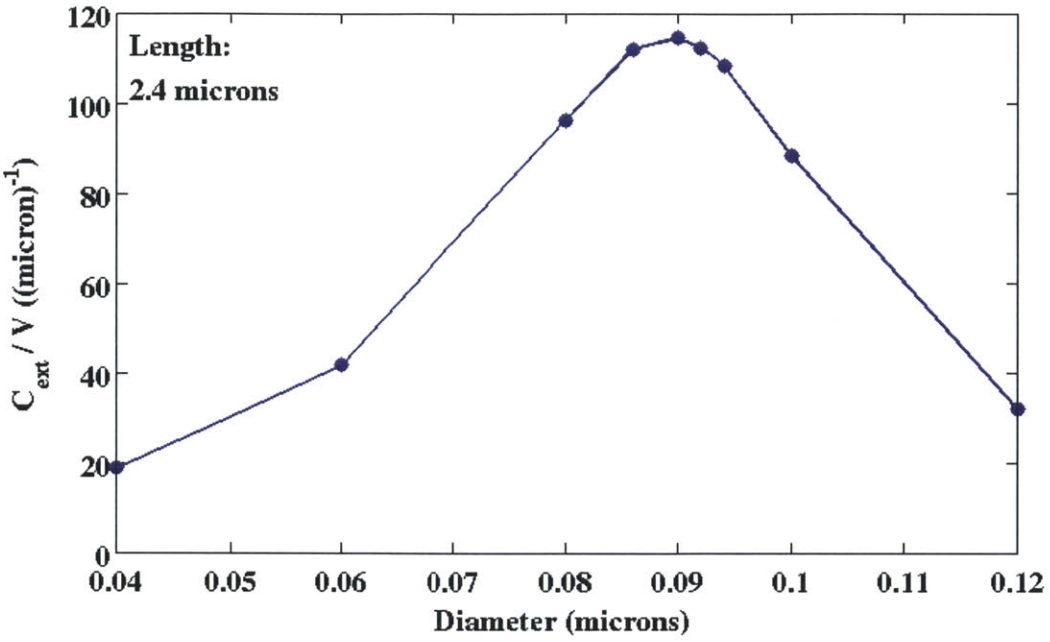

Figure 4-3: $\frac{C_{\text{ext}}}{V}$ optimization sweep of aluminum rods over equatorial diameter with the length fixed at 2400 nm; note that lines are merely to guide the eye and are not indicative of fitting or interpolation

the half-wavelength aluminum rod from [2] for $\lambda = 10\,\mu$m from [2], as that rod has $\frac{C_{\text{ext}}}{V} \approx 22\,(\mu\text{m})^{-1}$, while these optimized rods have $\frac{C_{\text{ext}}}{V} \approx 110\,(\mu\text{m})^{-1}$.

It should be possible to check the computed enhancement values against the quasistatic formula in equation 4.1 for rods, as the depolarization factors are known, as is ξ. The depolarization factors for a prolate ellipsoid with radii $r_1 \gg r_2 = r_3$ (so that $l = 2r_1$ and $D = 2r_2$) are $L_1 \approx \left(\ln\left(\frac{2r_1}{r_2} - 1\right)\right)\left(\frac{r_2}{r_1}\right)^2$ and $L_2 = L_3 = \frac{1-L_1}{2}$. Additionally, $p_1 = p_2 = p_3 = 1$ for ellipsoids. As an example, for the optimal rod

Table 4.1: Optimal Rod Extinctions ($h = \frac{D}{l}$)

Material	D (nm)	l (nm)	h^{-1}	$\frac{C_{\text{ext}}}{V}$ $((\mu\text{m})^{-1})$
Al	100	2640	26.4	113.978
Al	5	150	30	112.462
Al	90	2400	26.7	114.485
Ag	100	1900	19	66.7878
Ag	5	102	20.4	65.8244

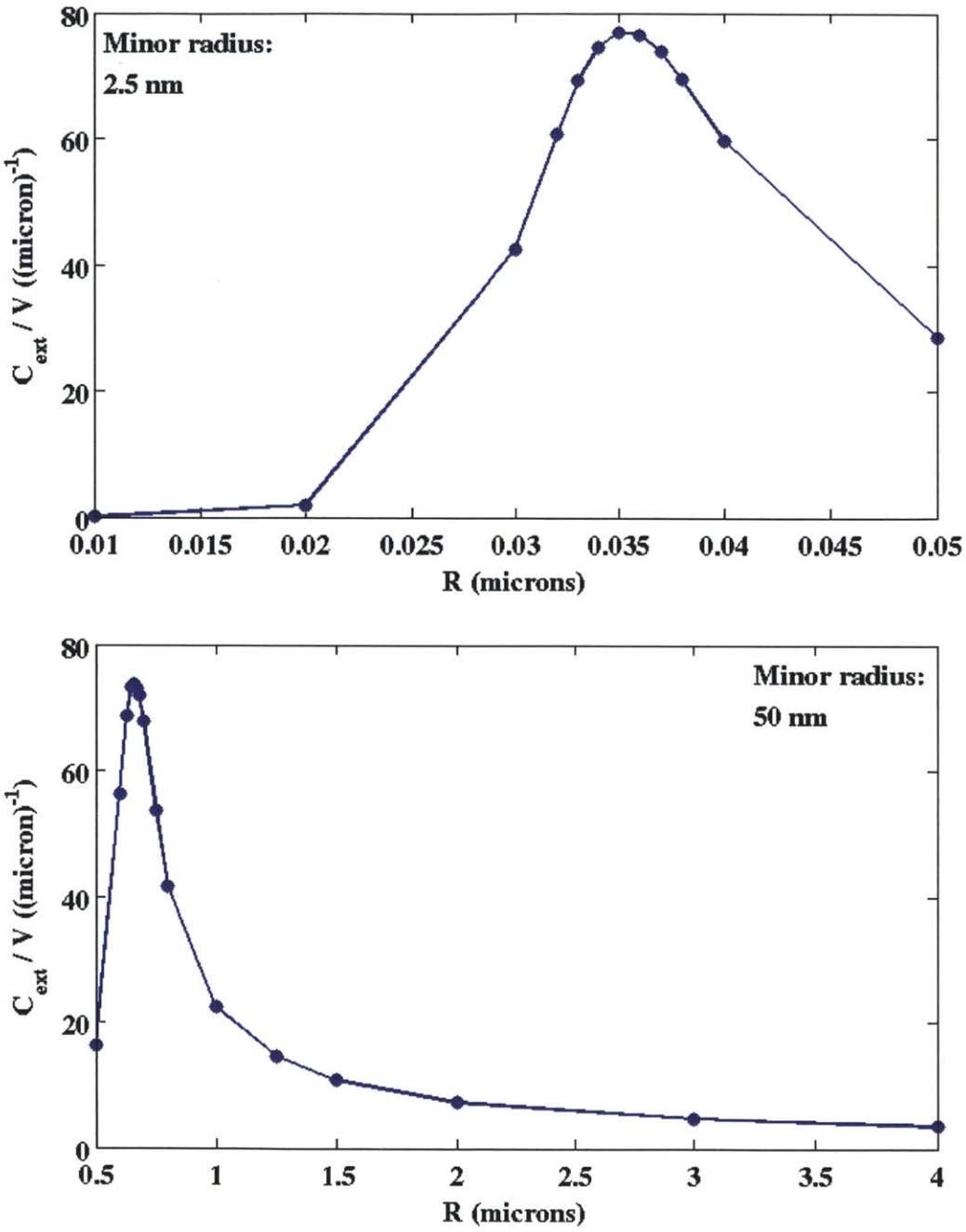

Figure 4-4: $\frac{C_{\text{ext}}}{V}$ optimization sweeps of aluminum tori over the major radius with the minor radius fixed; top: minor radius is 2.5 nm; bottom: minor radius is 50 nm; note that lines are merely to guide the eye and are not indicative of fitting or interpolation

of $r_1 = 1.32\,\mu$m and $r_2 = r_3 = 50\,$nm, then $L_1 \approx 0.00426$. If this rod is made of aluminum, then for $\lambda = 10\,\mu$m, then $\xi \approx 0.00272 + 0.00163i$ using the correction from equation 4.4. It is clear that $\xi_r \neq L_1$, yet this rod was computationally found

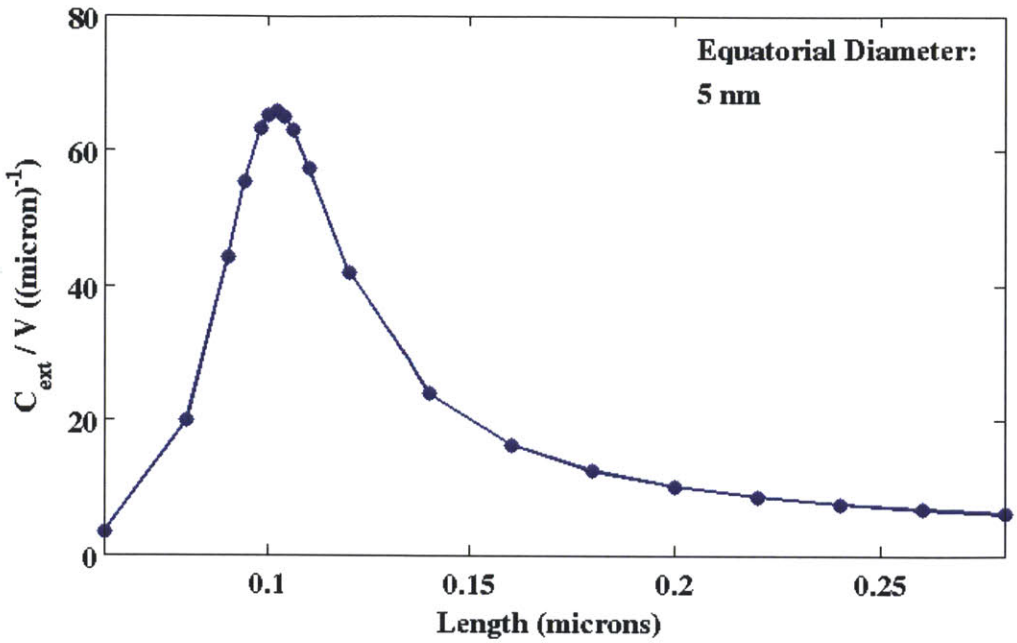

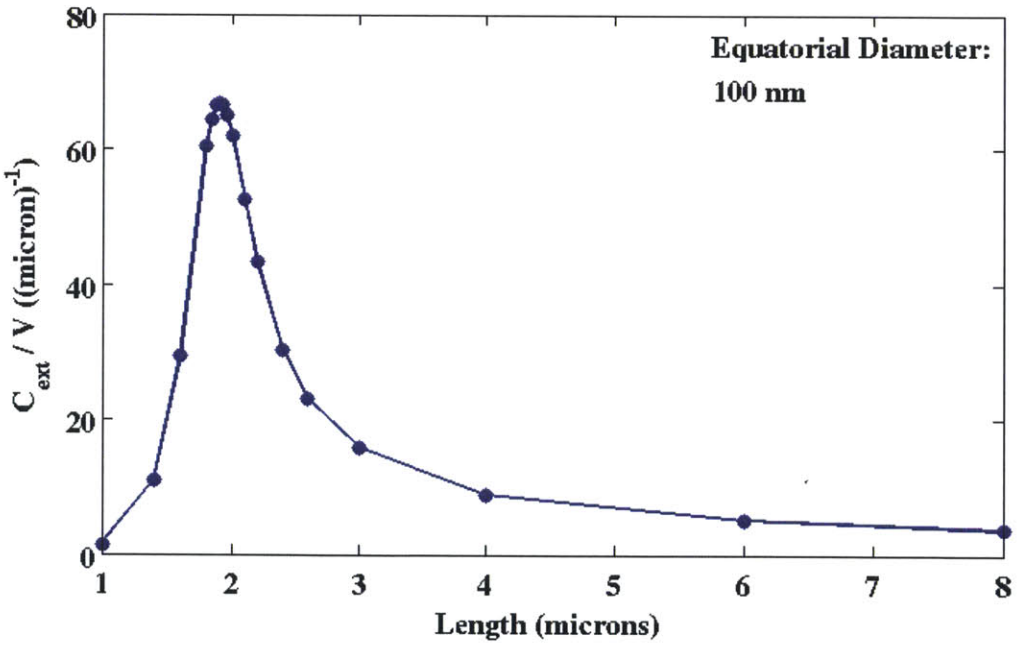

Figure 4-5: $\frac{C_{\text{ext}}}{V}$ optimization sweeps of silver rods over length with the equatorial diameter fixed; top: equatorial diameter is 5 nm; bottom: equatorial diameter is 100 nm; note that lines are merely to guide the eye and are not indicative of fitting or interpolation

to optimize $\frac{C_{\text{ext}}}{V}$. This implies that the rods with a length larger than 1 μm are not really quasistatic. This is corroborated by the fact that if the equation $L_1 = \xi_{\text{r}}$ is

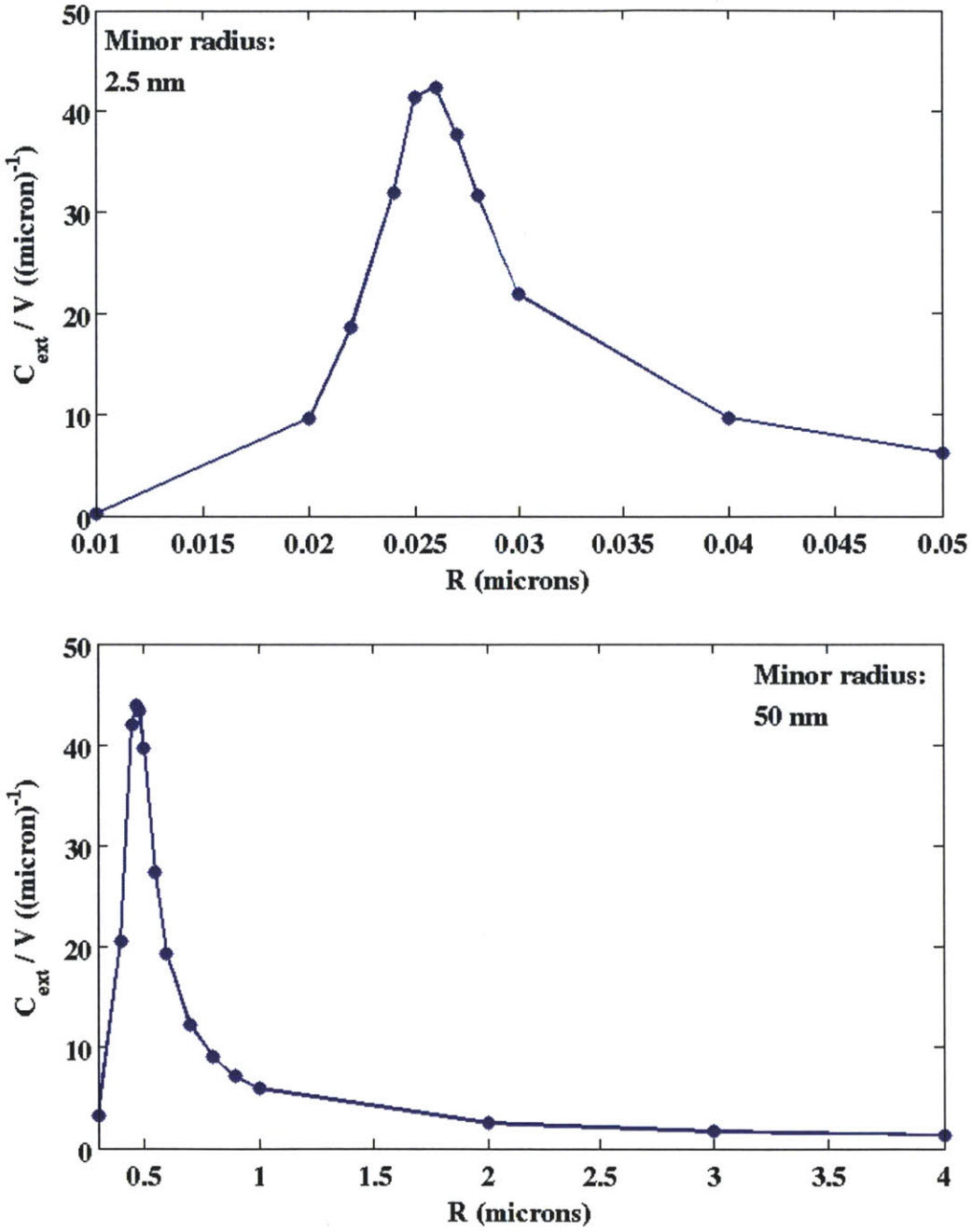

Figure 4-6: $\frac{C_{\text{ext}}}{V}$ optimization sweeps of silver tori over the major radius with the minor radius fixed; top: minor radius is 2.5 nm; bottom: minor radius is 50 nm; note that lines are merely to guide the eye and are not indicative of fitting or interpolation

solved for the length while keeping the diameter fixed at 100 nm, then the optimal length is 3.12 μm, which is essentially the result of assuming that even this long rod falls within the quasistatic regime. For such a rod, then $h^{-1} = 31.2$, and approximat-

Table 4.2: Optimal Torus Extinctions ($h = \frac{r}{\pi R}$)

Material	r (nm)	R (nm)	h^{-1}	$\frac{C_{\text{ext}}}{V}$ ($(\mu\text{m})^{-1}$)
Al	50	660	41.5	73.7225
Al	2.5	35	44.0	76.8535
Ag	50	470	29.5	43.9246
Ag	2.5	26	32.7	42.3449

ing equation 4.1 as $\frac{C_{\text{ext}}}{V} \approx \frac{2\pi}{3\lambda} \times \frac{1}{\xi_{\text{i}}}$ (accounting for equation 4.4 as usual) by only considering the contribution from $L_1 = \xi_{\text{r}}$ gives $\frac{C_{\text{ext}}}{V} \approx 109\,(\mu\text{m})^{-1}$; this can be done because the contributions from L_2 and L_3 in the sum are very small by comparison. Because this calculation is an approximation, it is most fair to say that the computed $\frac{C_{\text{ext}}}{V}$ values for the optimal aluminum rods appear to be approximately the same as this. Moreover, plugging $D = 100\,\text{nm}$ and $L = 3.12\,\mu\text{m}$ into equation 4.2 produces $\frac{C_{\text{ext}}}{V} \lesssim 220\,(\mu\text{m})^{-1}$, and that bound is double the value of $109\,(\mu\text{m})^{-1}$ found from the depolarization factors. This is to be expected because incident fields can only couple to the long axis of a prolate ellipsoid to excite surface charges and currents, while fields can couple to the two surface axes of an oblate ellipsoid, so as per [10], quasistatic oblate ellipsoids will generally be able to match the bound in equation 4.2 while quasistatic prolate ellipsoids will only attain half of the bound.

As another example, it is possible to check the above for the rod of length 150 nm and equatorial diameter 5 nm. In this case, $L_1 \approx 0.00344$ is much closer to $\xi_{\text{r}} \approx 0.00308$, and the contribution of L_1 to the bound in equation 4.2 gives $\frac{C_{\text{ext}}}{V} \approx 109\,(\mu\text{m})^{-1}$ again; this approximation comes from the computed structure, before trying to solve $L_1 = \xi_{\text{r}}$. Then, solving $L_1 = \xi_{\text{r}}$ for a fixed equatorial diameter of 5 nm and a variable length gives a length of 156 nm, which is significantly closer to the computed optimal structure and has $h^{-1} = 31.2$ and $\chi \approx -230 + 138i$ again. This gives the same bound of $\frac{C_{\text{ext}}}{V} \lesssim 220\,(\mu\text{m})^{-1}$ as in the previous paragraph, so again the attained value is half of the bound due to the bound being attainable by disks rather than rods. It would also seem that as the size of the rod increases, the optimal h^{-1} shifts below 31.2 calculated from the true quasistatic limit, while the optimized

$\frac{C_{ext}}{V} \approx 110\,(\mu\text{m})^{-1}$ remains roughly constant.

Returning now to the comparison of rods with disks, the depolarization factors for an oblate ellipsoid of radii $r_1 = r_2 \gg r_3$ are $L_1 = L_2 \approx \frac{\pi r_3}{4r_1}$ and $L_3 \approx 1 - \frac{\pi r_3}{2r_1}$, so L_1 and L_2 for an oblate ellipsoid involve a single factor of the aspect ratio, whereas L_1 for a prolate ellipsoid involves two factors of the aspect ratio. This implies that for the depolarization factors to be similar (leading to approximately similar performances in $\frac{C_{ext}}{V}$), an oblate ellipsoid would need $h^{-1} \approx 1000$ to be equivalent to a prolate ellipsoid with $h^{-1} \approx 30$. Disks of this aspect ratio cannot be manufactured at the quasistatic length scale, while manufacturing disks even with a thickness of 10 nm would then produce a face diameter of $10\,\mu$m; that is exactly equal to the wavelength of light considered, so such a disk would be far from quasistatic, and new models must be made to account for the absorption and scattering behaviors on that scale.

Therefore, in the infrared regime around $\lambda = 10\,\mu$m, the optimal structures that are manufacturable are aluminum rods, and the performance is roughly constant across length scales, from the quasistatic scale to the micron scale. Moreover, the performance is better than that of a half-wavelength aluminum rod.

4.4 Future Investigations

The parameter space examined in this thesis was very limited compared to what could be explored. The first extension would be to explore a larger range of the two dimensions over which rods and tori could be optimized. The second would be to consider multiple wavelengths and optimize structures for the average $\frac{C_{ext}}{V}$ over that range of wavelengths. Those two steps could be done using the same methods as have been used for this thesis.

The third extension would then be to consider a much larger space of shapes possible and optimize over those through shape calculus techniques. Based on results in [10], it is entirely possible that the optimal particles could have weird shapes compared to standard ellipsoids or tori, and could even have coatings made of different materials and thicknesses.

As noted in the previous section, disks are not considered because they would require much higher aspect ratios compared to rods to be able to provide comparable performance in $\frac{C_{ext}}{V}$, so they would not be manufacturable. The general rule of only considering structures that are "easy to manufacture" could then be formalized into a criterion on the smoothness of the particle surface, so that optimization of the particle shape and size would be subject to this smoothness constraint. On a broader scale, such a smoothness criterion could be used for many more photonic, metamaterial, and nanomechanical design problems. More relevant to this project, though, the smoothness criterion would likely produce optimal structures that have coatings, as coatings tend to reduce the aspect ratio of optimal structures with only small hits to performance in $\frac{C_{ext}}{V}$.

Chapter 5

Conclusions and Outlook

In this thesis, the work on simulating spontaneous emission enhancement atop a photonic crystal was done because not much work has been done yet for simulating quantum electromagnetic processes in classical electromagnetic solvers. By using MEEP to simulate quantum dipole transitions by classical stochastic dipoles, simulating spontaneous emission enhancement atop a photonic crystal compared to an untextured slab was successful, as it was validated by semianalytical predictions from [14], and those semianalytical predictions were separately validated by experimental results. Following this, it would be most useful to leverage the power of computational science to actually optimize photonic crystal structures for spontaneous emission enhancement. This could be done by manipulating both geometries and materials used. Moreover, basic crystal theory gives some ideas for what the band structure of a photonic crystal with a very high spectral density of states for certain modes would look like. The band structures of the photonic crystals directly optimized for spontaneous emission enhancement could be compared to those theoretically predicted. Additionally, as a cross-check, photonic crystals could be computationally modified to reproduce the band structure that would theoretically optimize the spectral density of states, and the performance in spontaneous emission enhancement could be compared to those structures that are directly optimized for this objective.

The success of stochastic electrodynamics when used in computational solvers as outlined above led to the simulation of an isolated nanoscale sphere, where the

top hemisphere radiates and the bottom hemisphere is a passive high-index material that behaves similarly to a metal in effectively reflecting significant fractions of incident light above. This structure was shown to have a significant enhancement of radiation detected above compared to below the sphere, as would theoretically be expected. Following this, similar spherical structures that reflect radiation in one direction could be considered, such as a nanoscale sphere that is homogeneously filled with radiating dipoles, but only one hemisphere is thinly coated with a metal. This could be generalized to the problem of optimizing the geometry of a nanoscale sphere for radiation in one direction versus another along the axis about which the system remains cylindrically symmetric.

Separately, aluminum rods when made at scales smaller (sometimes significantly so) than half of a wavelength were shown to outperform counterparts at half of a wavelength long when considering extinction in the infrared regime. This conclusion was reached by considering combinations of rod and torus shapes with aluminum and silver materials. While it seems like aluminum generally performs best at infrared extinction for any geometry, more general geometries could be considered through shape calculus techniques, leading to perhaps nonstandard optimal shapes compared to ellipsoids or tori. Moreover, optimal nanoparticles could be made of metals coated with other materials as well. These could arise because of general considerations about the smoothness of a shape, which dictates how easy it would be to manufacture nanoparticles of that shape. In fact, if a general criterion for smoothness could be come upon, that would have impacts far beyond optimization of nanoparticles for infrared extinction.

Appendix A

FDTD Spontaneous Emission Computation Code

As further detailed in [9], the Harminv algorithm decomposes a field profile over a range of frequencies into long-lived modes, giving the central frequency and lifetime of each mode, among other information; it works most efficiently when the field profile is made of only a small number of decaying sinusoids. The MEEP code used for finding modes through Harminv in the photonic crystal system studied in this thesis is detailed below. Additionally, the code used for FDTD enhancement computations is shared with the code used to run Harminv, so that is detailed below as well.

```
; materials
(include "materials.scm") ; list of material definitions

; material: si or custom material
(define-param custom-eps? true) ; flag if [noisy] Lorentzian
; susceptibility is used
(define-param w0 1e-4) ; Lorentzian susceptibility central frequency
; (value does not particularly matter as long as it is much closer
; to 0 than to resonant frequencies of the slab)
(define-param sigma0 1) ; Lorentzian susceptibility amplitude
```

```
(define-param gamma0 10) ; Lorentzian susceptibility linewidth
(define eps-func custom-eps) ; shortcut for calling Lorentzian
; susceptibility function

; dimension
(define-param 1d-slab? false) ; this is not a 1D calculation
(define-param 2d? true) ; this is a 2D calculation

; flag for Harminv mode-finding versus FDTD flux computation
(define-param harminv? false)

; geometry params (units of lscale)
(define-param computational-size 4) ; height of SiO substrate
; visible: this value is usually replaced as a parameter by 2
; to make the computational cell shorter and the calculations faster
(define a 321.4) ; length scale in nanometers
(define-param dpml 3.0) ; thickness of PML: this value is usually
; replaced as a parameter by 1 to make the computational cell shorter
; and the calculations faster
(define-param sin-thick (/ 250 a)) ; thickness of SiN slab (250 nm,
; converted to MEEP units by dividing by a)
(define sio-thick (+ dpml computational-size)) ; total height of SiO
; substrate (part of it is covered by PML)
(define-param hole-diameter (/ 161.7 a)) ; diameter of hole
; punched in SiN slab (161.7 nanometers)
(define Lx (* 2 sio-thick)) ; total computational cell should be
; 14 MEEP units long in the direction perpendicular to the slab area
(define sin-x (* 0.5 sin-thick)) ; SiN slab should be centered so
; that the bottom surface is at x = 0
(define sio-x (* -0.5 sio-thick)) ; SiO slab should be centered so
```

```
; that the top surface is at x = 0
(define-param meth-thick (/ 100 a)) ; active layer is 100 nm
(define meth-x (+ sin-thick (* 0.5 meth-thick))) ; active layer
; should be centered so that its top surface and the SiN
; slab top surface coincide

(define-param syz 1) ; computational cell is periodic along the y
; (and z, if relevant) directions with a periodicity of 1 MEEP
; unit of length
(define-param sy (if 1d-slab? 0 syz)) ; y-axis periodicity
(define-param sz (if (or 1d-slab? 2d?) 0 syz)) ; z-axis periodicity
; (if relevant)
(define-param output-ensemble? true) ; this will be true for
; FDTD flux calculations, where many of the same calculation
; will be done to average over random dipole configurations

(define-param flux-xcen (+ sin-x (* 0.5 sin-thick))) ; center of flux
; planes: this value is usually replaced by 1.7, which is above the
; active layer in this geometry (given the placement of the active
; layer and PML)

; polarization
(define-param pol Ex) ; current source excited, relevant only
; for Harminv: modes from Ez (Jz) are used in the final
; calculations, though modes from Ex (Jx) and Ey (Jy) are
; also checked to ensure that no modes are too close to each other
(print "field polarization = "pol"\n")

; ensure purely uniform slab geometry (irrelevant for 2D)
(if 1d-slab?
```

```
 (begin
  (set! sy 0)
  (set! sz 0)
  (set! 2d? false)
  (set! r 0)
 )
)

; calculation params
(set-param! resolution 20) ; resolution, unchanged
(define-param navg 1) ; number of ensembles to run - convergence found
; for navg = 100

(define-param Teq 500) ; time to wait for thermal equilibration,
; unchanged
(define-param T 2000) ; time to run collect fluxes: this is
; changed as a parameter to 100000 (10^5) for convergence

; modes were analyzed in FDTD flux calculations in a region of
; 6\omega/Q around the central frequency \omega, so fmin and fmax
; would be changed accordingly by passing different parameters:
; these bounds were also used when calculated the confinement factor
; from Harminv
(define-param nfreq 500) ; number of frequencies at which to
; compute flux (relevant only for FDTD flux calculations,
; irrelevant for Harminv): usually set as a parameter to
; 300
(define-param fmin 0.685) ; flux f_max
(define-param fmax 0.695) ; flux f_min
(define-param fcen (* 0.5 (+ fmin fmax))) ; center frequency for
```

```
; flux calculation
(define-param df (- fmax fmin)) ; frequency width for
; flux calculation

(print "geometry params: resolution = "
resolution", slab thickness = "h", dpml = "dpml"\n")
(print "computational params: T = "T", Teq = "Teq", nfreq = "
nfreq", fmin = "fmin", fmax = "fmax", navg = "navg"\n")

; thermal noise amplitude (for noisy Lorentzian susceptibility,
; actual value is less relevant; also note that noisy Lorentzian
; susceptibility is used only for FDTD flux calculation, while
; regular Lorentzian susceptibility is used for Harminv)
(define dx (/ 1 resolution))
(define dt (/ 0.5 resolution))
(define amp
 (if harminv? 0.0
  (sqrt (/ (* 8 pi) T dt
   (if 1d-slab? dx
    (if 2d? (* dx dx)
     (* 2 dx dx dx)
    )
   )
  )
  )
 )
)

; coordinates of single dipole source when performing Harminv:
; coordinates look rather random to excite all possible fields
```

```
; rather than only high-symmetry fields
(define src-cen-x 0.3234)
(define src-cen-y 0.2143)
(define src-cen-z 0.1132)
(define-param dT (* 1000 df)) ; time after fields are turned off
; before Harminv is performed: usually set to 10000 (10^4)
; as a parameter to allow for fields to decay sufficiently

(include "parallel.scm") ; allows for parallelizing the FDTD
; flux computations across many processors

; calls eps-func with parameters already set and with base
; dielectric constant as the only free parameter: this is a
; further shortcut definition of the noisy Lorentzian susceptibility
; function
(define (set-custom-eps epsinfo) (eps-func epsinfo w0 sigma0 gamma0 amp

; the following lines (up to the definitions of flux planes)
; are for making the FDTD flux calculations easier to parallelize
; across many processors by allowing computations at many k-points
; (where here only ky is varied): however, this is only used for
; Harminv with a broadband source, because the FDTD flux calculations
; are done around specific modes whose central frequencies and
; linewidths shift as k changes, so the FDTD flux calculations are only
; done for one value of ky at a time
; lists comprising external configurations
(define-param ky-min 0)
(define-param ky-max 0)
(define-param ky-interp 0)
(define ky-list
```

```
 (if (= ky-min ky-max)
  (list ky-min)
  (interpolate ky-interp (list ky-min ky-max))
 )
)
(define-param kz-min 0)
(define-param kz-max 0)
(define-param kz-interp 0)
(define kz-list
 (if (= kz-min kz-max)
  (list kz-min)
  (interpolate kz-interp (list kz-min kz-max))
 )
)
; make lists of internal/external work to do, assumed to be a direct
; product of internal = '(direct-product i1 i2 ...) and external =
; '(direct-product e1 e2 ...) lists.
(define internal-work '())
(define external-work '())
(if output-ensemble?
 (begin
  (set! external-work
   (direct-product ky-list kz-list (arith-sequence 1 1 navg))
  )
  (set! internal-work '(1))
 )
 (begin
  (set! external-work (direct-product ky-list kz-list))
  (set! internal-work (arith-sequence 1 1 navg))
 )
```

```
)

(define next (length external-work))
; number of (external) configurations
(define nint (length internal-work))
; number of runs per configuration
(define nsims (* next nint))
; total number of FDTD runs

(print "Computing a Total of "next" configurations with "
nint" computations per configuration\n")

(define ngroups (max 1 (min (meep-count-processors) nsims)))
(define mygroup (meep-divide-parallel-processes ngroups))

; list comprising both internal/external work
(define work
 (cdr
  (list-split
   (direct-product internal-work external-work) ngroups mygroup
  )
 )
)

; get the index of el in L, or false if el is not in L.
(define (get-index el L)
 (define (idx el L start)
  (if (null? L)
   #f
   (if (equal? el (car L))
```

```
    start (idx el (cdr L) (+ start 1))
   )
  )
 )
 (idx el L 0)
)

; next list of fluxes, each with nfreq entries
(define flux-left '()) ; list of fluxes (per frequency) from
; above the slab
(define flux-right '()) ; list of fluxes (per frequency) from
; below the slab
(define total-fluxes
 (make-vector next
  (arith-sequence 0.0 0.0 nfreq)
 )
) ; total of top and bottom fluxes (not really used due
; to sign issue and due to interest in top versus bottom flux)
(define total-topfluxes
 (make-vector next
  (arith-sequence 0.0 0.0 nfreq)
 )
) ; same as three lines above (technically a different
; object is needed though)
(define total-bottomfluxes
 (make-vector next
  (arith-sequence 0.0 0.0 nfreq)
 )
) ; same as three lines above (technically a different
; object is needed though)
```

```
; actually sets up and runs the flux calculation for each value of k
(map
 (lambda (w)
  (let*
   ((ew (cadr w)) ; external work parameters corresponding to run w
    (ewi (get-index ew external-work)) ; index of this ext.
    ; work in the external-work list
    ; external (configuration) parameters
    (ky (list-ref ew 0))
    (kz (list-ref ew 1))

   )

   ; set geometry
   ; computational cell should first be filled with
   ; passive nondispersive methanol of n = 1.33
   (set! default-material (make dielectric (index 1.33)))
   ; size of the computational cell (in 2D): note that the slab
   ; area is parallel to the the y-axis and the perpendicular
   ; (top/bottom) direction is the x-axis
   (set! geometry-lattice (make lattice (size Lx 1 no-size)))
   (set! geometry
    (list
     ; just in case, fill the computational cell again with
     ; passive nondispersive methanol ("infinity" means the
     ; full extent of the computational cell in that direction)
     (make block
      (center 0 0 0)
      (size Lx infinity infinity)
```

```
 (material (make dielectric (index 1.33)))
)
; then add the slab of passive nondispersive
; silicon nitride (n = 2.018)
(make block
 (center sin-x 0 0)
 (size sin-thick infinity infinity)
 (material (make dielectric (index 2.018)))
)
; then drill through the central axis of the silicon nitride
; with a cylindrical hole made of passive nondispersive
; methanol (this piece is omitted for the normalization
; calculation for the FDTD flux computation)
(make cylinder
 (center 0 0 0)
 (height Lx) (radius (/ hole-diameter 2)) (axis 1 0)
 (material (make dielectric (index 1.33)))
)

; second 100 nm thick methanol film (atop the slab)
; should be active with the same base index (1.33)
(make block
 (center meth-x 0 0)
 (size meth-thick infinity infinity)
 (material (set-custom-eps (* 1.33 1.33)))
)

; final piece is the silicon dioxide substrate
; below the silicon nitride slab
(make block
```

```
    (center sio-x 0 0)
    (size sio-thick infinity infinity)
    (material (make dielectric (index 1.45)))
   )

 )
)

; further ensure correct setup of geometry
(set! geometry
 (list-transform-negative geometry
  (lambda (o)
   (and
    (object-member? 'cylinder o)
    (zero? (object-property-value o 'radius))
   )
  )
 )
)
(set! k-point (vector3 0 ky kz)) ; periodic boundary conditions
; given k (here only ky varies, while kz = 0 always)
; PML of the desired thickness should only exist at the
; boundaries of the computational cell along the x-axis
(set! pml-layers
 (list (make pml (direction X) (thickness dpml)))
)
(if harminv?
 (begin
  ; source is a single dipole Gaussian pulse of desired
  ; frequency center and width, and unit amplitude (the
```

```
; absolute values of field and flux quantities in MEEP
; are far less relevant than properly-normalized ratios),
; which turns off after 5 time widths
(set! sources
 (list
  (make source
   (src (make gaussian-src (frequency fcen) (fwidth df)))
   (component pol) (size 0) (amplitude 1.0)
   (center src-cen-x src-cen-y 0)
  )
 )
)
; this runs Harminv over a range of ky values as taken
; from parameters, but has been commented out to allow
; narrowband Harminv calculations leading to calculation
; of the enhancement factor
;(run-k-points dT
 ;(interpolate ky-interp
  ;(list (vector3 0 ky-min 0) (vector3 0 ky-max 0))
 ;)
;)
;(exit) ; end program after a full loop of run-k-points
      (run-sources+ dT
       (at-beginning output-epsilon)
       (after-sources
        (harminv pol
         (vector3 src-cen-x src-cen-y 0) fcen df
        )
       )
```

```
    ;do not output power unless needed at the end
    (at-end
     output-efield-x
     output-efield-y
     output-efield-z
     output-hfield-x
     output-hfield-y
     output-hfield-z
     output-dpwr
     output-hpwr
     output-tot-pwr
    )
   )
  )
 (begin
   ; set polarizations: set all E-field components for FDTD flux
   (print "Flux calculation: setting sources\n")
   (set! sources
    (list
     (make source
      (src
       (make custom-src
        (src-func (lambda (t) 0.0))
        (end-time 0.0)
       )
      )
      (component Ex) (center 0) (size 0)
     )

     (make source
```

```
    (src
     (make custom-src
      (src-func (lambda (t) 0.0))
      (end-time 0.0)
     )
    )
    (component Ey) (center 0) (size 0)
   )

   (make source
    (src
     (make custom-src
      (src-func (lambda (t) 0.0))
      (end-time 0.0)
     )
    )
    (component Ez) (center 0) (size 0)
   )
  )
)
; equilibration run (wait to reach steady state)
(print "Flux calculation: just before equilibration\n")
(run-sources+ Teq)
(print "Flux calculation: just after equilibration,"
       "before setting flux sinks\n")
; adds flux planes above and below the slab
(set! flux-left
 (add-flux fcen df nfreq
  (make flux-region
   (center flux-xcen 0 0) (size 0 1 0)
```

```
  )
 )
)
(set! flux-right
 (add-flux fcen df nfreq
  (make flux-region
   (center (* -1 flux-xcen) 0 0) (size 0 1. 0)
  )
 )
)
(print "Flux calculation: after setting flux sinks,"
       "just before calculation\n")

(run-until T) ; flux planes calculated fluxes over time T

(print "Flux calculation: just after calculation,"
       "before vector-set total-fluxes\n")

; sets each flux plane data collection into
; the appropriate vector

(vector-set! total-topfluxes ewi
 (map
  (lambda (left total) (+ total left))
  (get-fluxes flux-left)
  (vector-ref total-topfluxes ewi)
 )
)
(vector-set! total-bottomfluxes ewi
 (map
```

```
            (lambda (right total) (+ total right))
            (get-fluxes flux-right)
            (vector-ref total-bottomfluxes ewi)
           )
          )
          (vector-set! total-fluxes ewi
           (map
            (lambda (left right total) (+ total left right))
            (get-fluxes flux-left)
            (get-fluxes flux-right)
            (vector-ref total-fluxes ewi)
           )
          )
        ))
    (reset-meep)
    ))
 work)

(if harminv?
 (print "Finished Harminv!\n")
 ; this part only executes for the FDTD flux calculation:
 ; it essentially processes the fluxes into a nice set of columns
 ; with associated frequencies
 (begin
  (print "Flux calculation: after vector-set total-fluxes,"
         "before do vector-set total-fluxes\n")
  (do ((i 0 (+ i 1))) ((= i next))
   (vector-set! total-fluxes i
    (map (lambda (f) (/ f (meep-count-processors)))
     (vector-ref total-fluxes i)
```

```
  )
 )
 (vector-set! total-topfluxes i
  (map (lambda (f) (/ f (meep-count-processors)))
   (vector-ref total-topfluxes i)
  )
 )
 (vector-set! total-bottomfluxes i
  (map (lambda (f) (/ f (meep-count-processors)))
   (vector-ref total-bottomfluxes i)
  )
 )
)
(meep-end-divide-parallel)
(define total-flux (arith-sequence 0.0 0.0 nfreq))
(define total-topflux (arith-sequence 0.0 0.0 nfreq))
(define total-bottomflux (arith-sequence 0.0 0.0 nfreq))
(define freqs (get-flux-freqs flux-left))

(do ((i 0 (+ i 1))) ((= i next))
 (vector-set! total-fluxes i
  (map (lambda (f) (meep-sum-to-all f))
   (vector-ref total-fluxes i)
  )
 )
 (vector-set! total-topfluxes i
  (map (lambda (f) (meep-sum-to-all f))
   (vector-ref total-topfluxes i)
  )
 )
```

```
(vector-set! total-bottomfluxes i
 (map (lambda (f) (meep-sum-to-all f))
  (vector-ref total-bottomfluxes i)
 )
)
(set! total-flux
 (map (lambda (f t) (+ f t))
  (vector-ref total-fluxes i)
  total-flux
 )
)
(set! total-topflux
 (map (lambda (f t) (+ f t))
  (vector-ref total-topfluxes i)
  total-topflux
 )
)
(set! total-bottomflux
 (map (lambda (f t) (+ f t))
  (vector-ref total-bottomfluxes i)
  total-bottomflux
 )
)

(display-csv
 (string-append "flux" (number->string i))
 freqs
 (vector-ref total-fluxes i)
 (vector-ref total-topfluxes i)
 (vector-ref total-bottomfluxes i)
```

```
    )
   )
   (map
    (lambda (i ev) (print "external-work" i ":")
     (map (lambda (v) (print ", " v)) ev)
     (print "\n")
    )
    (arith-sequence 0 1 next)
    external-work
   )
  )
)

(sleep 2)
```

The code for simulating the "half-sphere" is very similar to the above but with the geometry, dimensions, and boundary conditions changed appropriately, so it will not be included here. The two auxiliary files to make this program work are listed below. The first, called as "materials.scm", contains the relevant material definitions used.

```
; Define dispersive glass / fluid dielectric functions
(define-param length-scale 1e-6)
; default to units of 1 micron for these definitions
(define-param c 2.99792458e8) ; speed of light
; base unit is 2*pi*c/a, so divide by this much
; to get omega in MEEP units
(define wconv (/ length-scale c (* 2 pi)))

; TODO: MEEP now admits
; (E-polarizations (list of susceptibilities))
```

```
; LIST OPERATIONS

; perform pointwise operation (op) on members of two lists
(define (list-op op l1 l2)
  (if (number? l2)
      (if (number? l1)
          (op l1 l2)
          (map (lambda (x) (op x l2)) l1))
      (if (number? l1)
          (map (lambda (x) (op x l1)) l2)
          (if (= (length l1) (length l2))
              (map (lambda (x y) (op x y)) l1 l2)
              '()))))

; square list
(define (list-sqr l1)
  (if (number? l1)
      (sqr l1)
      (map (lambda (x) (sqr x)) l1)))

; MATERIAL DEFINITIONS

; shortcut for calling Lorentzian
; susceptibility with parameters
(define (make-lorentzian w0 sigma0 gamma0)
  (make lorentzian-susceptibility
    (omega w0) (sigma sigma0) (gamma gamma0)))

; shortcut for calling noisy Lorentzian
; susceptibility with parameters
```

```
(define (make-noisy-lorentzian w0 sigma0 gamma0 amp)
  (if (= amp 0)
      (make lorentzian-susceptibility
        (omega w0) (sigma sigma0) (gamma gamma0))
      (make noisy-lorentzian-susceptibility
        (noise-amp amp) (omega w0) (sigma sigma0) (gamma gamma0))))

; material definition for gold (Au)
(define (gold amp)
  (let* ((einf 1)
         (w0 1e-6)
         (wp (* 1.37e16 wconv))
         (sigma0 (/ (* wp wp) (* w0 w0)))
         (gamma0 (* 5.317e13 wconv)))
    (if (= amp 0)
        (make medium (epsilon einf)
              (E-polarizations
               (make-lorentzian w0 sigma0 gamma0)))
        (make medium (epsilon einf)
              (E-polarizations
               (make-noisy-lorentzian w0 sigma0 gamma0 amp))))))

; noisy Lorentzian susceptibility with custom index and parameters:
; eps(w) = epsinf + sigma * w0^2 / (w0^2 - w^2 - 1i*gamma0*w)
; where the user inputs f0 = w0/(2*pi), Gamma0 = gamma0/(2*pi)
; and sigma into the lorentzian function
(define (custom-eps epsinf w0 sigma0 gamma0 amp)
  (if (= amp 0)
      (make medium (epsilon epsinf)
            (E-polarizations
```

```
            (make-lorentzian (/ w0 (* 2 pi))
                             (/ sigma0 w0 w0)
                             (/ gamma0 (* 2 pi)))))
      (make medium (epsilon epsinf)
            (E-polarizations
             (make-noisy-lorentzian (/ w0 (* 2 pi))
                                    (/ sigma0 w0 w0)
                                    (/ gamma0 (* 2 pi))
                                    amp)))))
```

The second, called as "parallel.scm", contains code allowing for parallelization of a computation with multiple ensemble runs across multiple processors in a node of a computing cluster.

```
; direct product of lists: a list of lists,
; containing (e1 e2 ..) for every e1 in L1
; and every e2 in L2, etcetera
(define (direct-product . Ls)
 (define (direct-product2 L1 L2)
  (apply append
   (map (lambda (e1)
    (map (lambda (e2) (list e1 e2)) L2)) L1)))
  (cond
   ((null? Ls) '())
   ((= (length Ls) 1) (car Ls))
   ((= (length Ls) 2) (direct-product2 (car Ls) (cadr Ls)))
   (else (map
          (lambda (el)
          (cons (car el) (cadr el)))
          (direct-product2 (car Ls)
           (apply direct-product (cdr Ls)))))))
```

```
; Split a list L into num more-or-less equal pieces,
; returning the piece given by index (in 0..num-1),
; along with the index in L of the first element of
; the piece, as a car pair: (first-index . piece-of-L).
(define (list-split L num index)
 (define (list-sub L start len index rest)
  (if (null? L)
   (reverse rest)
   (if (and (>= index start) (< index (+ start len)))
    (list-sub (cdr L) start len (+ index 1) (cons (car L) rest))
    (list-sub (cdr L) start len (+ index 1) rest))))
   (if (or (>= index num) (negative? index))
    (cons (length L) '())
    (let ((block-size (quotient (+ (length L) num -1) num)))
    (let ((start (* index block-size))
    (len (min block-size (- (length L) (* index block-size)))))
    (cons start (list-sub L start len 0 '()))))))
```

Appendix B

BEM Scattering Codes

Below is an example SCUFFGEO file. It lists the dielectric function for aluminum. (Two are listed, but only one, which is the one in [2], is used.) Additionally, it lists which geometric object/mesh should have the aluminum dielectric function associated with it. By default, it sets the exterior region to be the vacuum.

MATERIAL Al

```
eps0 = 8.854e-12;
tau = 8.88e-15;
sigma0 = 2.81e7;
waistrad = 4.6e-2;
longrad = 1.2;
Eps(w) = 1 - (waistrad * sigma0)/(eps0 * w *
         (longrad + waistrad) * (tau * w + i));
```

ENDMATERIAL

MATERIAL AlDrudeRakic

```
eVtoW = 1.519100e15;
```

```
  EpsInf = 1;
  wp = 2.3245e16;
  gamma = 9.0913e14;
  waistrad = 5e-2;
  longrad = 2;
  Eps(w) = EpsInf - (waistrad * wp^2) / ((waistrad +
           longrad) * ( w^2 + i*gamma*w ));

ENDMATERIAL

OBJECT TheAlRodFiber
  MESHFILE RodFiber.msh
  MATERIAL Al
ENDOBJECT
```

Below is the code used to calculate angle- and polarization-averaged $\frac{C_{ext}}{V}$ values for each structure. Note that the axes are rotated for this rod, as it lies along the x-axis, so the coordinate system is rotated as well. This is not the case for the tori, as the tori lie in the xy-plane, but aside from those differences, the code is otherwise the same. The parameters to be specified are the SCUFFGEO file, the list of frequencies, and the maximum spherical polar angle (along with the maximum azimuthal angle if azimuthal symmetry is absent, though this is not the case for the systems considered in this thesis).

```
#include <cstdlib>
#include <iostream>
#include "libscuff.h"
#include "cubature.h"

using namespace scuff;
```

```
typedef struct {
    RWGGeometry *G;
    HMatrix *M;
    HVector *KN;
    HVector *rhs_neg_omega;
    cdouble Omega;
    double vol;
    double solid_angle;
} sv_data;

// calculate the volume of an RWGGeometry
double Volume(RWGGeometry *G)
{
    double vol = 0.0, *x0, *x1, *x2, xc[3];
    // xc a dummy variable for VecCross
    RWGSurface *S;
    RWGPanel *P;
    for(int ns=0; ns<G->NumSurfaces; ++ns) {
        S = G->Surfaces[ns];
        if( !S->IsClosed )
            Warn("Volume may be meaningless; at least" +
                 "one surface does not close on itself");
        for(int np=0; np<S->NumPanels; ++np) {
            P = S->Panels[np];
            x0 = S->Vertices + 3*P->VI[0];
            x1 = S->Vertices + 3*P->VI[1];
            x2 = S->Vertices + 3*P->VI[2];
            VecCross(x1,x2,xc);
            vol += (1.0/6.0)*VecDot(x0,VecCross(x1,x2,xc));
```

```
        }
    }
    return vol;
}

// calculate extinction at surface, with panel quantities
//      we assume RHS = RHS(-omega), which equals conj(RHS)
//      if omega=real
cdouble CalcExtSurf(HVector *KN, HVector *RHS)
{
        cdouble PExt (0.0, 0.0);
        double Sign = 1.0;
        for(int nr=0; nr<KN->N; ++nr, Sign*=-1.0)
        {
                PExt += -0.5 * ZVAC * Sign *
                 RHS->GetEntry(nr) * KN->GetEntry(nr);
        }
        PExt *= (cdouble) 2.0*ZVAC;
        // normalizing to incident power 1/(2*ZVAC)
        return PExt;
}

int sigma_angle(unsigned ndim, const double *x,
                void *fdata, unsigned fdim, double *fval)
{
    double theta = x[0];
    double phi = (ndim==2) ? x[1] : 0;
    double nHat[3] = {cos(theta), cos(phi) * sin(theta),
                      sin(phi) * sin(theta)};
    cdouble E0[3] = {-sin(theta), cos(phi) * cos(theta),
```

```
                        sin(phi) * cos(theta)};
    cdouble E1[3] = {0, -sin(phi), cos(phi)};
    // define spherical coordinates

    // set up problem for BEM solution for each polarization
    sv_data *svd = (sv_data *) fdata;
    PlaneWave PW = PlaneWave(E0, nHat);
    svd->G->AssembleRHSVector(svd->Omega, &PW, svd->KN);
    svd->M->LUSolve(svd->KN);
    svd->G->AssembleRHSVector(cdouble(-1.0) * svd->Omega,
                              &PW, svd->rhs_neg_omega);
    cdouble sv1 = CalcExtSurf(svd->KN, svd->rhs_neg_omega)
                  / svd->vol;

    PW.SetE0(E1);
    svd->G->AssembleRHSVector(svd->Omega, &PW, svd->KN);
    svd->M->LUSolve(svd->KN);
    svd->G->AssembleRHSVector(cdouble(-1.0) * svd->Omega,
                              &PW, svd->rhs_neg_omega);
    cdouble sv2 = CalcExtSurf(svd->KN, svd->rhs_neg_omega)
                  / svd->vol;

    fval[0] = 1. / svd->solid_angle * sin(theta) *
              (real(sv1) + real(sv2)) / 2.;
    return 0;
}

// set phi_min=phi_max=0 to integrate only over theta
int main(int argc, char **argv) {
    if (argc<4) {
```

```
    std::cerr << "Usage: scuff-sim-angleavg"
                 "GeoFile OmegaFile ThetaMax"
        " [PhiMax]" << std::endl;
    exit(EXIT_FAILURE);
}

// input parameters
const char *geo_file = argv[1];
const char *omega_file = argv[2];
double theta_max = atof(argv[3]);
unsigned ndim;
double phi_max;
if (argc==4) {
    ndim = 1;
    phi_max = 0;
} else {
    ndim = 2;
    phi_max = atof(argv[4]);
}

double theta_min = 0;
double phi_min = 0;

// integration over (theta, phi) (or just theta)
double *xmin = new double[ndim];
double *xmax = new double[ndim];
xmin[0] = theta_min;
xmax[0] = theta_max;
if (ndim==2) {
    xmin[1] = phi_min;
```

```
    xmax[1] = phi_max;
}
double solid_angle = 1 - cos(theta_max);
if (ndim==2)
    solid_angle *= phi_max;

// cubature (numerical integration) parameters
const unsigned fdim = 1; // sigma_per_vol
const double rel_error = 1.e-3;
const double abs_error = 0;
const size_t max_eval = 1e5;
double err[fdim];

RWGGeometry *G = new RWGGeometry(geo_file);
HMatrix *M = G->AllocateBEMMatrix();
HVector *KN = G->AllocateRHSVector();
HVector *rhs_neg_omega = G->AllocateRHSVector();
HVector *OmegaList = new HVector(omega_file, LHM_COMPLEX);
double *sigma_per_vol = new double[OmegaList->N];
double vol = Volume(G);

sv_data svd = {G, M, KN, rhs_neg_omega, 0, vol, solid_angle};
for (int i=0; i<OmegaList->N; ++i) {
    cdouble omega = OmegaList->GetEntry(i);
    //std::cout << "omega: " << omega << std::endl;
    svd.Omega = omega;
    // find Cext/V for each angle and polarization and numerically
    // integrate to find angle- and polarization-averaged Cext/V
    G->AssembleBEMMatrix(omega, M);
    M->LUFactorize();
```

```
        hcubature(fdim, sigma_angle, &svd, ndim, xmin, xmax,
                  max_eval, abs_error, rel_error,
                  ERROR_L2, sigma_per_vol + i, err);
        std::cout << sigma_per_vol[i] << std::endl;
    }

    return 0;
}
```

Bibliography

[1] `http://homerreid.com/scuff-EM`.

[2] Paul G Appleyard. Modelled infrared extinction and attenuation performance of atmospherically disseminated high aspect ratio metal nanoparticles. *Journal of Optics A: Pure and Applied Optics*, 9(3):278, 2007.

[3] C. Bohren and D. R. Huffman. *Absorption and Scattering of Light by Small Particles.* Wiley Science Paperback Series, 1983.

[4] Misha Boroditsky, Rutger Vrijen, Thomas F. Krauss, Roberto Coccioli, Raj Bhat, and Eli Yablonovitch. Spontaneous emission extraction and purcell enhancement from thin-film 2-d photonic crystals. *J. Lightwave Technol.*, 17(11):2096, Nov 1999.

[5] David L. C. Chan, Marin Soljačić, and J. D. Joannopoulos. Direct calculation of thermal emission for three-dimensionally periodic photonic crystal slabs. *Phys. Rev. E*, 74:036615, Sep 2006.

[6] Shanhui Fan and J. D. Joannopoulos. Analysis of guided resonances in photonic crystal slabs. *Phys. Rev. B*, 65:235112, Jun 2002.

[7] M. T. Homer Reid and S. G. Johnson. Efficient Computation of Power, Force, and Torque in BEM Scattering Calculations. *ArXiv e-prints*, July 2013.

[8] John D. Joannopoulos, Steven G. Johnson, Joshua N. Winn, and Robert D. Meade. *Photonic Crystals: Molding the Flow of Light (Second Edition)*, chapter 2-3. Princeton University Press, 2 edition, 2008.

[9] Vladimir A. Mandelshtam and Howard S. Taylor. Harmonic inversion of time signals and its applications. *The Journal of Chemical Physics*, 107(17):6756–6769, 1997.

[10] O. D. Miller, C. W. Hsu, M. T. H. Reid, W. Qiu, B. G. DeLacy, J. D. Joannopoulos, M. Soljačić, and S. G. Johnson. Fundamental limits to extinction by metallic nanoparticles. *Phys. Rev. Lett.*, 112:123903, Mar 2014.

[11] A. F. Oskooi, D. Roundy, M. Ibanescu, P. Bermel, J. D. Joannopulos, and S. G. Johnson. MEEP: A flexible free-software package forelectromagnetic simulations

by the FDTD method. *Computer Physics Communications*, 181:687–702, January 2010.

[12] Ardavan F. Oskooi, A. Taflove, and S. G. Johnson. *Advances in FDTD Computational Electrodynamics: Photonics and Nanotechnology*, chapter 4. Artech House, Norwood, MA, 2013.

[13] S. M. Rytov. *Theory of Electric Fluctuations and Thermal Radiation.* Air Force Cambridge Research Labs, Hanscom Air Force Base, MA, Jul 1959.

[14] Bo Zhen, Song-Liang Chua, Jeongwon Lee, Alejandro W. Rodriguez, Xiangdong Liang, Steven G. Johnson, John D. Joannopoulos, Marin Soljačić, and Ofer Shapira. Enabling enhanced emission and low-threshold lasing of organic molecules using special fano resonances of macroscopic photonic crystals. *Proceedings of the National Academy of Sciences*, 2013.